PRODUCTION AND CHARACTERIZATION OF
MULTILAYERED ONE DIMENSIONAL PLASMONIC
NANOWIRES

A THESIS SUBMITTED TO
THE GRADUATE SCHOOL OF NATURAL AND APPLIED SCIENCES
OF
THE MIDDLE EAST TECHNICAL UNIVERSITY

BY

EZGİ AYGÜN

IN PARTIAL FULFILLMENT OF THE REQUIREMENTS
FOR
THE DEGREE OF MASTER OF SCIENCE
IN
MICRO AND NANOTECHNOLOGY

AUGUST 2017

Approval of the thesis:

PRODUCTION AND CHARACTERIZATION OF
MULTILAYERED ONE DIMENSIONAL PLASMONIC NANOWIRES

submitted by **EZGİ AYGÜN** in partial fulfillment of the requirements for the degree of **Master of Science in Micro and Nanotechnology Department**, **Middle East Technical University** by,

Prof. Dr. Gülbin Dural Ünver
Dean, Graduate School of **Natural and Applied Sciences**   _____

Assoc. Prof. Dr. Burcu Akata Kurç
Head of Department, **Micro and Nanotechnology**   _____

Assoc. Prof. Dr. Alpan Bek
Supervisor, **Department of Physics, METU**   _____

Assoc. Prof. Dr. H. Emrah Ünalan
Co-Supervisor, **Metallurgical and Materials Eng., METU**   _____

Examining Committee Members:

Assoc. Prof. Dr. Akın Bacıoğlu
Physics Engineering Dept., Hacettepe University   _____

Assoc. Prof. Dr. Alpan Bek
Department of Physics, METU   _____

Prof. Dr. Ali Çırpan
Department of Chemistry, METU   _____

Assoc. Prof. Dr. Hande Toffoli
Department of Physics, METU   _____

Assoc. Prof. Dr. Engin Durgun
Institute of Materials Science and Nanotechnology, Bilkent Uni.   _____

Date: 16/08/2017

I hereby declare that all information in this document has been obtained and presented in accordance with academic rules and ethical conduct. I also declare that, as required by these rules and conduct, I have fully cited and referenced all material and results that are not original to this work.

Name, Last name: Ezgi Aygün

Signature:

ABSTRACT

PRODUCTION AND CHARACTERIZATION OF
MULTILAYERED ONE DIMENSIONAL PLASMONIC
NANOWIRES

Aygün, Ezgi

M.Sc., Department of Micro and Nanotechnology
Supervisor: Assoc. Prof. Dr. Alpan Bek
Co-Supervisor: Assoc. Prof. Dr. H. Emrah Ünalan

August 2017, 90 pages

In this study, the main objective is to obtain enhanced optical properties from low dimensional nanostructures via tailoring their plasmonic properties. As the low dimensional multilayered plasmonic structures bear hybrid plasmon modes due to plasmon mixing, some of these modes are found to be subject to very low attenuation, resulting in long range and long lifetime plasmons. Such nanostructures have the potential to be utilized as efficient light management interfaces in thin film photovoltaic devices or as low-loss interconnects in integrated photonic circuitry. For this purpose, a novel geometry was designed composed of one dimensional (1D) metal/dielectric multilayers.

Scattering spectra of multilayered nanostructures depend strongly on the thicknesses of the layers. Atomic layer deposition (ALD) technique was used to deposit thin titanium dioxide (TiO_2) spacer layers on high aspect ratio polyol synthesized core silver nanowires. The ALD process was optimized by investigating the compositional, morphological, optical, and electrical properties of the deposited thin films using various characterization techniques.

A thin layer of silver on top of TiO_2 coated silver nanowires serves as a coaxial outer layer facilitating plasmon hybridization. The optical characterization of the resultant nanowires indicates that the plasmonic response of 1D coaxial nanowires of metal-dielectric-metal multilayers can be tuned by tailoring the constituent layers. In this study, we showed that it is possible to generate new hybridized plasmon modes in 1D multilayered nanowires.

Keywords: Coaxial Nanowires, Atomic Layer Deposition, Titanium Dioxide, Plasmonic Interfaces

ÖZ

ÇOK KATMANLI TEK BOYUTLU PLAZMONİK NANOTELLERİN ÜRETİMİ VE İNCELENMESİ

Aygün, Ezgi

Yüksek Lisans, Mikro ve Nanoteknoloji Bölümü

Tez Yöneticisi: Doç. Dr. Alpan Bek

Ortak Tez Yöneticisi: Doç. Dr. H. Emrah Ünalan

Ağustos 2017, 90 sayfa

Bu tez çalışmasında temel amaç, düşük boyutlu nanoyapıların plazmonik özelliklerinin uyarlanması yoluyla iyileştirilmiş optik özellikler elde etmektir. Düşük boyutlu ve çok katmanlı nanoyapılar melez plazmon kiplerini desteklediklerinden, oluşan bu kiplerden bir kısmı oldukça düşük sönümlenmeye maruz kalır ve ortaya uzun menzilli ve uzun ömürlü plazmonlar çıkar. Bu nanoyapıların ince film fotovoltaik aygıtlarda ışık yönlendirici arayüzler ya da tümleşik fotonik devre ara bağlantıları gibi alanlarda kullanım potansiyeli bulunmaktadır. Bu amaçla, tek boyutlu metal ve dielektrik katmanlardan oluşan yeni bir geometri tasarlanmıştır.

Çok katmanlı nanoyapıların saçılma izgeleri nanoyapıyı oluşturan katmanların kalınlıklarıyla yakından ilişkilidir. Yüksek boy/en oranlı, polyol tekniğiyle sentezlenmiş gümüş nanotellerin üzerine dielektrik titan dioksit (TiO_2) ince filmlerin kaplanmasında atomik katman yığma (ALD) tekniği kullanılmıştır. ALD işlemi, çeşitli teknikler kullanılarak ince filmlerin bileşimsel, biçimsel, optik ve elektriksel özelliklerinin incelenmesi yoluyla eniyileştirilmiştir.

TiO$_2$ kaplı gümüş nanotellerin üzerine kaplanan ince bir gümüş katman plazmon melezleşmesine yardımcı olmuştur. Elde edilen nanotellerin optik incelenmesi göstermiştir ki metal-dielektrik-metal katmanlardan oluşan tek boyutlu eş eksenli nanotellerin plazmonik özellikleri, nanoteli oluşturan katmanların uyarlanmasıyla ayarlanabilmektedir. Bu çalışmada, çok katmanlı tek boyutlu nanotellerde yeni melez plazmon kiplerinin oluşturulabileceği gösterilmiştir.

Anahtar Kelimeler: Eş Eksenli Nanoteller, Atomik Katman Yığma, Titan Dioksit, Plazmonik Arayüzler

Dedicated to my family

ACKNOWLEDGMENTS

I would like to express my endless love to my gorgeous family for their love and trust in me. I am very lucky to have them.

My final words go to my beloved husband for holding my hand so tightly in good and bad times. He means all to me.

TABLE OF CONTENTS

LIST OF TABLES

LIST OF FIGURES

FIGURES

LIST OF ABBREVIATIONS

ABBREVIATIONS

1D	One Dimensional
AFM	Atomic Force Microscopy
ALD	Atomic Layer Deposition
CVD	Chemical Vapor Deposition
GIXRD	Grazing Incidence X-Ray Diffraction
GPC	Growth Per Cycle
LSPR	Localized Surface Plasmon Resonance
MIM	Metal/Insulator/Metal
NP	Nanoparticle
NW	Nanowire
PVP	Polyvinylpyrrolidone
RMS	Root Mean Square
SE	Spectroscopic Ellipsometry
SEM	Scanning Electron Microscopy
SP	Surface Plasmon
SPP	Surface Plasmon Polariton
SPR	Surface Plasmon Resonance
TDMAT	Tetrakis(dimethylamido)titanium
TE	Transverse-Electric
TM	Transverse-Magnetic
TMA	Trimethylaluminum
XPS	X-Ray Photoelectron Spectroscopy

CHAPTER 1

INTRODUCTION

Plasmonics is an emerging research field which is based on exploiting the nanoscale properties of metals. Metals support surface plasmons that are characterized by a resonant frequency. The surface plasmons can be either localized in the metal surface as for metal nanoparticles or propagating as for planar metal surfaces. By tailoring the metal nanostructure geometry, surface plasmon resonance or plasmon propagation properties can be tuned for different applications [1]. The utilization of surface plasmons plays an important role for better photon harvesting due to the strong scattering mechanism into the active materials and the guiding of light at the metal/dielectric interface [2].

Thin film solar cells are presently considered as alternative to conventional solar cells in the research of low cost photovoltaics. However, the photoactive layer needs to be reduced in order to achieve low cost, which in turn causes efficiency loss in these cells. Therefore, the light trapping effect or the increase in the amount of light scattered into the substrate become crucial for efficiency enhancement. By decorating the surface of the thin film solar cells with plasmonic nanostructures, better scattering and light trapping properties can be obtained [1]. One dimensional (1D) metal-dielectric-metal nanowires are good candidates in this manner. They can increase the amount of light scattered into the active layer as well as trapping the light inside the spacer dielectric layer via surface plasmon polaritons.

In electronic integrated circuits, it is desired to confine the electric field tightly in low dimensional structures for faster signal processing with broader bandwidth. One dimensional metal nanowires are promising due to their subwavelength diameters, high aspect ratios, low sidewall roughness, and high refractive indices. However, a metal nanowire waveguide has to work in the proximity of its surface plasmon resonance frequency, which mostly results in high propagation loss [3]. On the other hand, integrating several dielectric / metal multilayers on top of metal nanowires can

facilitate hybridized plasmon modes between the metal layers. A high refractive index dielectric material between the core and the claddings provides strong light confinement to the waveguide core [4]. These coaxial nanowires can serve as low-loss waveguides in integrated photonic circuitry.

The major source of optical losses in optical waveguides is light scattering at surface imperfections. Atomic layer deposition (ALD) is a thin film deposition technique consisting of sequential self-limiting surface reactions, providing atomically flat surfaces. Therefore, thin films produced by ALD can eliminate the light scattering due to surface roughness and enable low-loss signal processing [4].

In this thesis, one dimensional metal-dielectric-metal nanowires were produced. ALD technique was used to deposit thin layers of titanium dioxide (TiO_2) on top of one dimensional core silver nanowires. Due to the self-limiting nature of the ALD process, the TiO_2 coatings around the silver nanowires were perfectly conformal. A thin layer of silver was deposited on top of TiO_2 deposited silver nanowires.

Aluminum oxide (Al_2O_3) has a lower refractive index compared to TiO_2. To investigate the effect of the refractive index of the dielectric layer on plasmonic properties, coaxial nanowires with ALD Al_2O_3 were also produced using the same production steps.

Hybridized plasmon modes were observed from the resultant coaxial nanowires. These new hybridized plasmon modes are expected to be beneficial in light management applications.

CHAPTER 2

PLASMONIC EFFECTS

2.1 A Brief History

Plasmonics is the study and application of the interaction between electromagnetic radiation and free electrons in a metal. This kind of interaction induces collective electron oscillations inside the metal. Plasmon can be defined as quanta of these plasma oscillations and can result in unique optical properties. The usage of metal nanostructures without knowing about plasmonic effects dates back to the fourth century AD, to the Roman Empire, with *Lycurgus Cup* which is shown in Figure 2.1(a). This ancient piece of art has become famous due to its unique response to light; it has a green color when reflecting light and shines in red in transmitting light conditions. Other examples that unknowingly use plasmons are church window glasses generating brilliant colors which can be seen in Figure 2.1(b).

Figure 2.1 (a) The Lycurgus cup, and (b) colored windows designed by Marc Chagall for All Saints' Church in Kent, England.

Michael Faraday was the first scientist who conducted controlled experiments to examine the interaction of light with metal particles in the mid-1850s. He was fascinated when he observed the ruby color of colloidal gold solution and he called it *activated gold* [5]. His study is recognized as the birth of modern nanotechnology [6]. This was followed by Zsigmondy's work in which he managed to observe colloidal gold particles using the ultramicroscope he had invented [7].

In 1865, James Clark Maxwell proposed the theory of light as an electromagnetic wave [8]. The German physics professor Gustav Mie had a strong background in mathematics and solved Maxwell's equations to explain scattering of light by spherical gold nanoparticles [9]. His 1908 paper is the basis of aerosol optics [10]. He provided an explanation for the ruby-red color of colloidal gold solutions, showing resonant structures in the scattering spectra which we now know as plasmon resonances.

The term *plasmon* was first proposed by David Pines and David Bohm in 1952 to describe high frequency collective electron oscillations inside metals [11]. Since the electron density in metals is much higher than in gaseous plasmas, the plasma frequency in metals is much higher. Plasmon is the quantization of these plasma oscillations. Since plasma oscillations travel as longitudinal waves through the metal, these excitations cannot couple with light as light is a transverse wave. However, the excitations which we now call volume or bulk plasmons, can be excited by high energy electrons. Accordingly, the theory of plasmons was developed in order to explain characteristic electron energy losses when electrons pass through different metals. In 1957, Rufus Ritchie published a work in which he examined plasma losses in thin films [12]. Martin Fleischmann and his co-workers reported very large enhancement of Raman scattering for molecules adsorbed on a roughened silver electrode and ascribed the effect to the large surface area of the adsorbed molecules [13]. It was later shown that the enhancement in the Raman signals was due to the strongly enhanced local electromagnetic fields produced by surface plasmons and the phenomenon was named "Surface Enhanced Raman Scattering" (SERS) [14].

The interest in plasmonics has emerged significantly in the end of the 20th century with the discovery of *extraordinary optical transmission* (EOT) by Ebbesen et al. [15]. The new phenomenon revealed the greatly enhanced transmission of light through sub-wavelength holes on thick metal films. The enhancement was attributed to the existence of different surface plasmon modes that occurs in the metallic holes. This

phenomenon indicated the possibility of confinement and control of light in the sub-nanometer scale and gave rise to the plasmonic studies significantly.

2.2 Theoretical Considerations

Before going into details of plasmonics, it is worth mentioning what *plasma* is. Plasma is a system of mobile charged particles which interact with one another via Coulombic forces. This system can be considered as a gas of negatively charged free electrons moving against a fixed massive background of positive ions, atomic cores. The electrons have a large kinetic energy even at low temperatures whereas the massive (positive) ions have a little. As a result, the collective oscillations of the (positive) ions (i.e., phonons) and the crystal structure are entirely dominated by the electrons [16].

An explanation for the optical properties of metals can be made by a *plasma model* over a wide frequency range since the sea of electrons in a metal tends to form a plasma. The free electron gas is driven by an external electric field in the plasma model. The electromagnetic response of a plasma to an oscillating electric field is the movement of negatively charged particles apart from the positively charged background, the so-called polarization. The electrons oscillate at the *plasma frequency* until their energy is lost, a phenomenon called *damping*, due to collisions occurring with a characteristic collision frequency. The plasma frequency is in the ultraviolet region for most metals, as will be explained below, ranging between 5-15 eV [17].

The optical response of a metal to an impinging light wave is governed by its plasma frequency, explaining an everyday phenomenon. It is well known from everyday life that metals exhibit shiny appearance. The reason for that behavior is that metals are highly reflective for frequencies up to the visible part of the optical spectrum, which are smaller than the plasma frequencies of metals, prohibiting electromagnetic waves propagate through them. In this low-frequency regime (e.g., far-infrared, microwave) metals are recognized as perfect or good conductors since only a negligible part of the incident electromagnetic waves is able to penetrate. At higher frequencies, closer to the visible region of the spectrum, electric field penetration increases significantly, giving rise to dissipation. At even higher frequencies, i.e. ultraviolet frequencies, metals gain dielectric character allowing electromagnetic wave propagation with some extent of attenuation depending on the electronic band structure of the metal. While

alkali metals are transparent in this regime because of their free-electron-like response, noble metals such as silver or gold exhibit strong absorption due to the transitions between their electronic bands [17].

The dispersive properties of metals can be described via a complex, frequency-dependent dielectric function $\varepsilon(\omega) = \varepsilon_1(\omega) + i\varepsilon_2(\omega)$. At optical frequencies, ε can be determined by solving the complex refractive index equation:

$n(\omega) = n(\omega) + i\kappa(\omega) = \sqrt{\varepsilon}.$

This yields

$$\varepsilon_1 = n^2 - \kappa^2 \tag{2.1}$$

$$\varepsilon_2 = 2n\kappa \tag{2.2}$$

$$n^2 = \frac{\varepsilon_1}{2} + \frac{1}{2}\sqrt{\varepsilon_1^2 + \varepsilon_2^2} \tag{2.3}$$

$$\kappa = \frac{\varepsilon_2}{2n}. \tag{2.4}$$

The real part of the refractive index n determines the dispersion in the medium whereas κ is the extinction coefficient determining the optical absorption of propagating electromagnetic waves. The extinction coefficient is linked to the absorption coefficient α through Beer's law ($I(x) = I_0 e^{-\alpha x}$) by the relation

$$\alpha(\omega) = \frac{2\kappa(\omega)\omega}{c}. \tag{2.5}$$

The imaginary part ε_2 of the complex dielectric function is therefore responsible for the amount of absorption inside the medium [17]. A more detailed explanation for the dielectric function will be given in the following subsection.

2.2.1 Dielectric Function of Metals

The dielectric function $\varepsilon(\omega)$ can be obtained exploiting a plasma model for metals known as the *Drude model*. Here, the motion of electrons of effective mass m and concentration N is damped through a characteristic collision frequency $\gamma = 1/\tau$. Here, τ is the relaxation time of the free electron gas, that is the average time between

successive collisions. The value of τ is typically around 10^{-14} s at room temperature, which corresponds to a collision frequency of 100 THz [17].

An electric field gives rise to polarization to give the electric displacement in a medium. This relation can be written as [14]

$$\boldsymbol{D} = \varepsilon_0\boldsymbol{E} + \boldsymbol{P} = \varepsilon_0\varepsilon(\omega)\boldsymbol{E} \tag{2.6}$$

in terms of the relative permittivity (dielectric constant) of the medium ε where $\boldsymbol{D}$, $\boldsymbol{E}$ and $\boldsymbol{P}$ are the vectors of electric displacement, electric field, and polarization, respectively. For an electron in the plasma under an external electric field $\boldsymbol{E}$, the equation of motion is given as:

$$m\frac{d^2x}{dt^2} + m\gamma\frac{dx}{dt} = -e\boldsymbol{E} \tag{2.7}$$

If the harmonic time dependence of the driving force is described as $\boldsymbol{E}(t) = \boldsymbol{E_0}e^{-i\omega t}$, the electron oscillation can be described via $\boldsymbol{x}(t) = \boldsymbol{x_0}e^{-i\omega t}$. The complex amplitude $\boldsymbol{x_0}$ incorporates any possible phase shift between the driving force and the response as

$$\boldsymbol{x}(t) = \frac{e}{m(\omega^2 + i\gamma\omega)}\boldsymbol{E}(t). \tag{2.8}$$

The macroscopic polarization caused by the displaced electrons $\boldsymbol{P} = -Ne\boldsymbol{x}$, is then:

$$\boldsymbol{P} = -\frac{Ne^2}{m(\omega^2 + i\gamma\omega)}\boldsymbol{E}. \tag{2.9}$$

Inserting this relation into Equation (2.1) yields

$$D = \varepsilon_0 \left(1 - \frac{Ne^2}{\varepsilon_0 m(\omega^2 + i\gamma\omega)} \right) E \qquad (2.10)$$

and one arrives at the expression for complex dielectric function $\varepsilon(\omega)$,

$$\varepsilon(\omega) = 1 - \frac{Ne^2}{\varepsilon_0 m(\omega^2 + i\gamma\omega)} \qquad (2.11)$$

$$\varepsilon(\omega) = 1 - \frac{\omega_p^2}{\omega^2 + i\gamma\omega} = 1 - \frac{\omega_p^2 \tau^2}{\omega^2 \tau^2 + i\omega\tau} \qquad (2.12)$$

with the notation of plasma frequency ω_p,

$$\omega_p^2 = \frac{Ne^2}{\varepsilon_0 m}. \qquad (2.13)$$

One can now clearly see that since N is approximately 10^{23} cm^{-3} for typical metals such as silver or copper [18], the plasma frequency ω_p is in the ultraviolet region.

The real and imaginary components of the dielectric function $\varepsilon(\omega) = \varepsilon_1(\omega) + i\varepsilon_2(\omega)$ can be given by

$$\varepsilon_1(\omega) = 1 - \frac{\omega_p^2 \tau^2}{1 + \omega^2 \tau^2} \qquad (2.14)$$

$$\varepsilon_2(\omega) = \frac{\omega_p^2 \tau}{\omega(1 + \omega^2 \tau^2)} \qquad (2.15)$$

where $\gamma = 1/\tau$ is used.

For low frequencies where $\omega \ll \tau^{-1}$, $\varepsilon_2 \gg \varepsilon_1$; metals are strongly absorbing, retaining their metallic character. It is therefore wise to consider the $\omega < \omega_p$ region while examining equations (2.14) and (2.15).

In case of large frequencies $\omega > \omega_p$, the approximation $\omega\tau \gg 1$ is valid. The damping term $i\omega\tau$ can then be neglected and $\varepsilon(\omega)$ becomes predominantly real:

$$\varepsilon(\omega) = 1 - \frac{\omega_p^2}{\omega^2} \tag{2.16}$$

This high frequency region is known as the transparency regime for metals in which they do not retain their metallic character. It should be noted that the behavior of noble metals (e.g. Au, Ag, Cu) in this high frequency regime is changed by interband transitions. Interband transitions occur when the material is subjected to photons with energies larger than the threshold of transitions between electronic bands. As a result, ε_2 increases and strong absorption occurs.
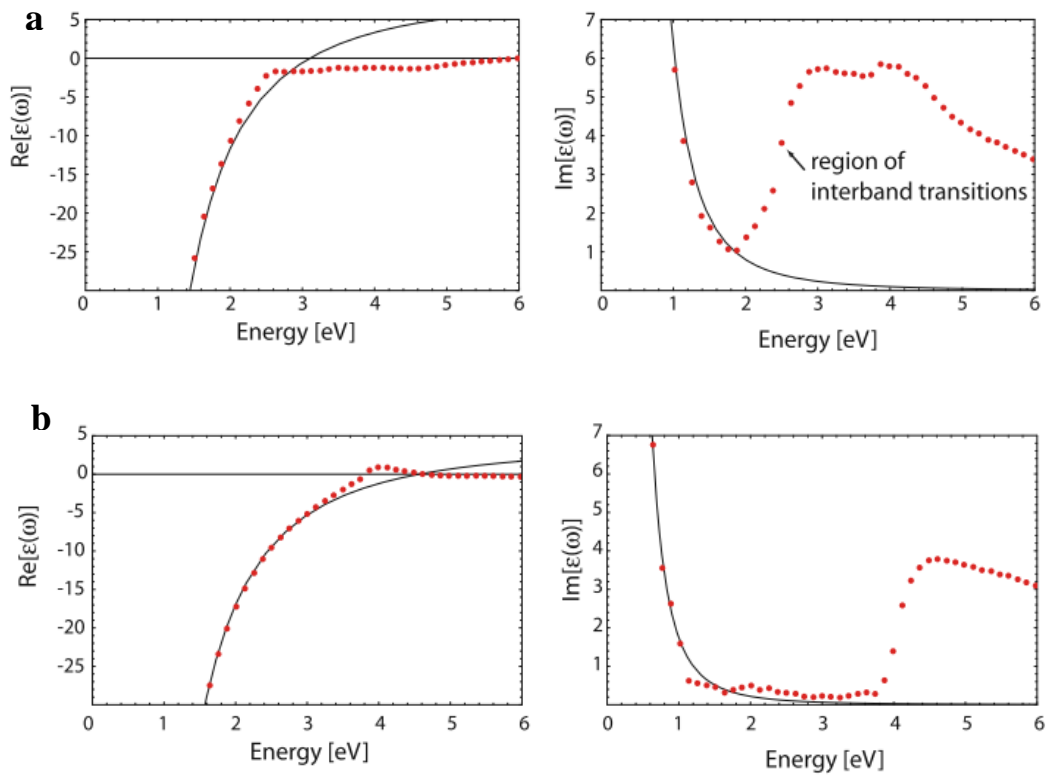
Figure 2.2 The real and imaginary part of $\varepsilon(\omega)$ (dots) and a Drude model fit to the data (a) for gold and (b) for silver [17].

For some noble metals such as silver and gold, interband effects begin to occur at energies above 1 eV. As an example, the real and imaginary parts $\varepsilon_1(\omega)$ and $\varepsilon_2(\omega)$ for gold and silver and their Drude model fits are illustrated in Figure 2.2 [17]. For the case of gold, the break down occurs at visible frequencies, leading to an increase in ε_2 and making Drude model inadequate. For silver, however, the model seems to be valid at visible frequencies.

2.2.2 Localized Surface Plasmons

An electromagnetic wave impinging on a metal surface only has a certain penetration depth (<50 nm for Ag and Au); therefore, the electrons on the surface are the most significant [19].

Surface plasmon resonance (SPR) is a critical consideration in applications exploiting surface plasmons. The intensity and the position of SPR depend on nanostructure shape, size, and composition; and the dielectric medium surrounding the nanostructures [20]. Therefore, SPR can be tailored by optimizing the design of the nanostructures. There are two different cases for SPR: localized SPR (LSPR) and propagating surface plasmon polaritons (SPPs).

LSPR is generated by a light trapped within conductive nanoparticles (NPs) smaller than the wavelength of light as shown in Figure 2.3(a). The phenomenon is induced by the interactions between the incident light and surface electrons in a conduction band [21].
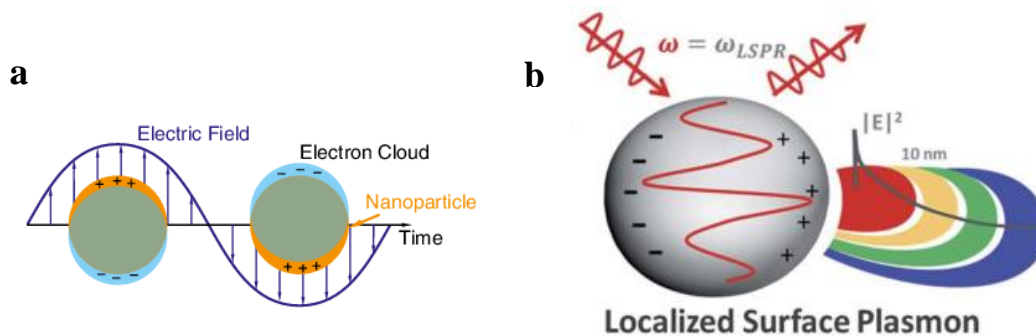
Figure 2.3 Schematic of localized surface plasmon resonance (LSPR) showing (a) the oscillating electric dipole induced by a light trapped within conductive nanoparticles (NPs) and (b) the decaying nature of the LSPR.

LSPR is meaningful for particles larger than~15 nm because smaller particles induce strong quantum effects. Figure 2.3(b) demonstrates that the electromagnetic field changes with distance and the LSPR decays between ~10-30 nm. It is possible to excite the LSPR directly by the incident field since the nanoparticle geometry (i.e. zero-dimensional NP) supplies additional momentum; therefore, there is no momentum matching conditions [20].

2.2.3 Surface Plasmon Polaritons

Surface plasmon polaritons (SPPs) are electromagnetic excitations that propagate along the dielectric - metal interface, and evanescently confined in the perpendicular direction. These surface waves arise from the coupling of the electromagnetic fields to electron oscillations inside the metal. SPPs can propagate on the surface for tens to hundreds of micrometers and eventually decay due to the absorption in the metal and scattering in the dielectric medium [17].

The composed character of an SPP generated at the metal-dielectric interface is presented in Figure 2.4(a). The local EM field induced by the SPP can extend up to 200 nm into the dielectric medium (Figure 2.4(b)). Therefore, if the dielectric medium changes within this distance, the SPP frequency will also shift [20].
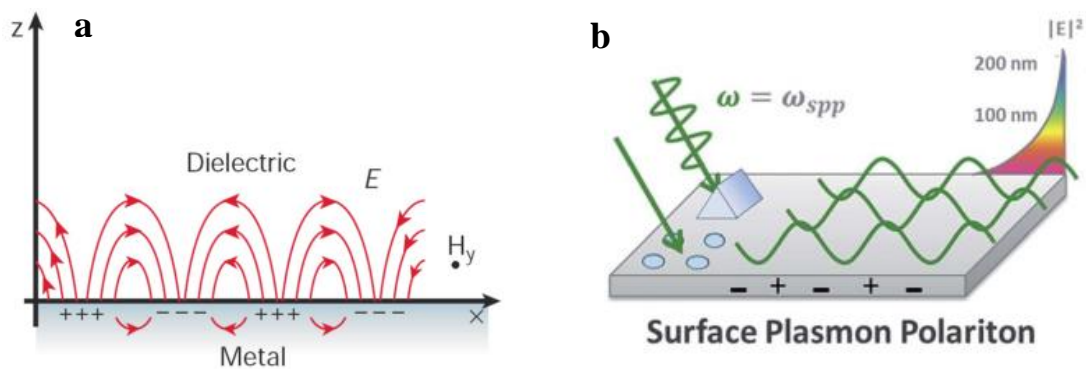
Figure 2.4 (a) The composed character of SPPs generated at the metal-dielectric interface, and (b) the extention of the local EM field into the dielectric [20].

The simplest geometry sustaining SPPs is that of a single interface of a semi-infinite metal and a semi-infinite dielectric with complex dielectric functions of ε_m and ε_d, respectively. Analysis of Maxwell's equations suggests that no surface modes exist for transverse-electric (TE) polarization. Therefore, SPPs can only exist for transverse-magnetic (TM) polarization and its vector of intensity of magnetic field lies in the plane of metal-dielectric interface which is perpendicular to the direction of propagation [17]. If the Cartesian system of coordinates is chosen such as the metal occupies the region $z < 0$ and the SPP propagates along the x-direction, the vector of magnetic intensity $\vec{H}$ of the SPP is given by

$$\vec{H}_j = (0, H_y, 0)_j = (0,1,0)A \exp[-\alpha_j z + i(\beta x - \omega t)] \qquad (2.17)$$

where j is either m for metal or d for dielectric, ω is the angular frequency, t is time, β is the propagation constant, $\alpha_j = \sqrt{\beta^2 - (\omega/c)^2 \varepsilon_j}$, and $i = \sqrt{-1}$. The electric field vector is perpendicular to the magnetic intensity vector and can be calculated from Maxwell's equations and Equation (2.17) [22].

The spatial distribution of the magnetic intensity is presented in Figure 2.5. The figure shows that the magnetic field intensity peaks at the metal-dielectric interface and decays into the dielectric and metal media. The field decay that is perpendicular to the metal-dielectric interface is defined by the penetration depth. It is also defined as the distance from the interface at which the amplitude of the field decreases by a factor of e. The penetration depth is affected by the wavelength and permittivities of the materials involved [22].
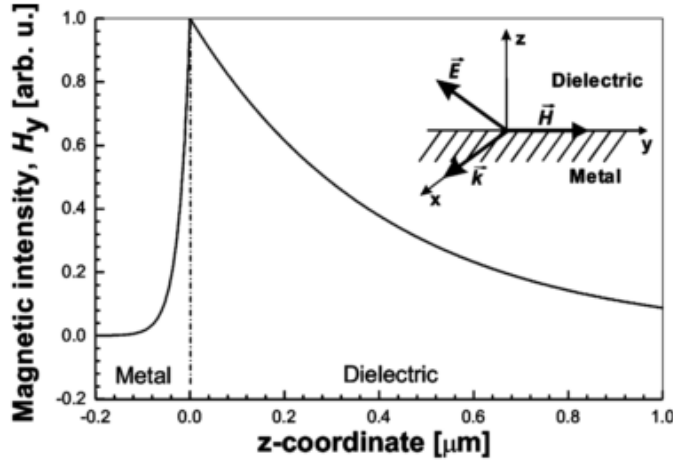
Figure 2.5 Spatial distribution of the magnetic intensity for an SPP at the interface between gold and a dielectric of $\eta_d = 1.328$, where $\lambda = 850$ nm [22].

2.2.3.1 Propagation of Surface Plasmon Polaritons

Whereas light propagating in a free space has a linear dispersion ($\omega = ck$) between the frequency (ω) and momentum (k), the SPP mode at a metal-dielectric interface has momentum larger than the free-space photon. The propagation constant at a metal-dielectric interface can be given as

$$\beta = k_{SPP} = k_0 \sqrt{\frac{\varepsilon_d\, \varepsilon_m}{\varepsilon_d + \varepsilon_m}} = \frac{\omega}{c} \sqrt{\frac{\varepsilon_d\, \varepsilon_m}{\varepsilon_d + \varepsilon_m}} \qquad (2.18)$$

where k_0 is defined as the wave vector of the free-space light, λ is the wavelength in a vacuum, ε_d and ε_m are the permittivities of the metal and the surrounding dielectric medium, respectively [22]. Dispersion relation of a surface plasmon mode is presented in Figure 2.6, which reveals the momentum mismatch between the photons and surface plasmon polaritons. Since the wave vector or the momentum of the SPP is always greater than the wave vector of the massless photon, SPP cannot be directly excited by the incident light [20].

If the structure is lossless ($\text{Im}[\varepsilon_m] = \text{Im}[\varepsilon_d] = 0$), Equation (2.18) represents a guided mode only if the permittivities $\text{Re}[\varepsilon_m]$ and $\text{Re}[\varepsilon_d]$ are of opposite signs and $\text{Re}[\varepsilon_m] < -\,\text{Re}[\varepsilon_d]$. Since dielectric materials usually have positive permittivities, the metal must have a negative real part of permittivity. Silver and gold are known to have a negative real part of permittivity in the visible and near-infrared regions. They also have a considerable imaginary part of permittivity, which results in a nonzero imaginary part of the propagation constant of a surface plasmon. The imaginary part of the propagation constant is responsible for the attenuation of the surface plasmon in the propagation direction [22].
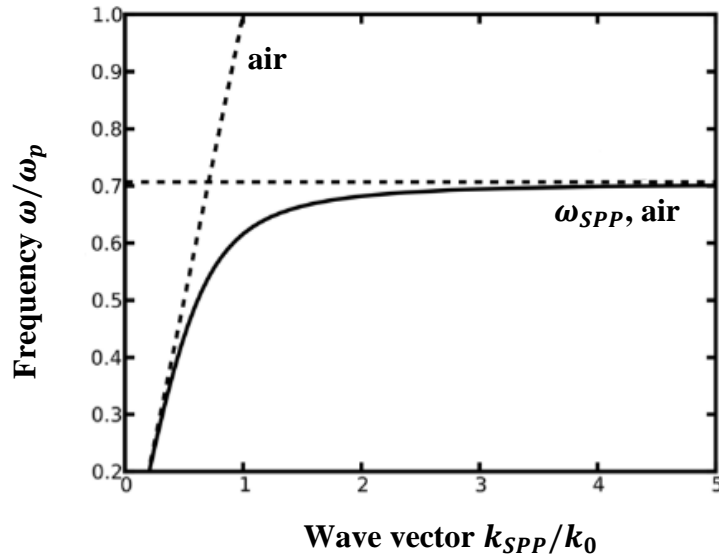
Figure 2.6 Dispersion relation of a SPP mode. The dashed line shows the dispersion line of light in free space.

2.3 Nanowire Plasmonic Waveguides

Recently, one dimensional (1D) metallic nanostructures are of great interest because of their distinct electrical, optical, magnetic, and thermal properties when compared to their bulk counterparts. Especially bottom-up synthesized 1D metallic nanowires usually exhibit perfectly uniform diameters down to tens of nanometers and extremely smooth surfaces. Due to their single crystal nature, subwavelength diameters, low sidewall roughness, high refractive indices and high aspect ratios, these nanowires offer great opportunities as plasmonic waveguides with deep-subwavelength confinement, coherence maintenance and low scattering losses [3].

By coupling the light to surface plasmon polaritons at the surface of the metal nanowire, electromagnetic waves at optical frequencies can be tightly confined at the metal-dielectric interface. On the other hand, such a metal waveguide needs to work in the proximity of its surface plasmon resonance frequency to provide deep-subwavelength confinement, which usually results in high Ohmic losses due to strong electron-phonon interactions. However, it is possible to minimize the losses in a plasmonic waveguide by optimizing the geometry, composition or guiding wavelength [3].

The propagation of a surface plasmon polariton has been discussed in subsection 2.2.3.1. In order to define propagation and confinement properties of a SPP the following parameters hold importance. The propagation constant defined in Equation (2.18) is related to the effective index n_{ef} as

$$n_{ef} = \frac{c}{\omega} Re\{\beta_{SP}\} \qquad (2.19)$$

and therefore the effective index can be defined as the ratio of the propagation constant in the waveguide to the free space propagation constant. The propagation length of the plasmon modes can be defined as

$$L = \frac{1}{2} Im\{\beta_{SP}\}. \qquad (2.20)$$

Besides the propagation loss, another important parameter of the plasmon mode in a waveguide is the effective mode area A, which can be defined by the ratio of a mode's total energy density per unit length and its peak energy density,

$$A = \frac{1}{max\{W(r)\}} \int_{A_\infty} W(r) dA \qquad (2.21)$$

where $W(r)$ is the energy density

$$W(r) = \frac{1}{2} Re\left\{\frac{d[\omega\varepsilon(r)]}{d\omega}\right\} |E(r)|^2 + \frac{1}{2}\mu_0 |H(r)|^2. \qquad (2.22)$$

Here $|E(r)|^2$ and $|H(r)|^2$ are the intensity of electric and magnetic fields, respectively. $\varepsilon(r)$ and μ_0 are the electric and free space magnetic permittivities.

2.3.1 One Dimensional Silver Nanowires

Silver nanowires (Ag NWs) with well-defined dimensions are particularly interesting to study because bulk silver has the highest electrical (or thermal) conductivity among all metals [23]. Therefore, Ag NWs have been utilized in applications such as catalysis [24], surface-enhanced Raman scattering (SERS) [25], photonic crystals [26], biological nanosensors [27], and plasmonic waveguides [28]–[30].

The silver (and also gold) systems are unique because their surface plasmon resonance frequencies are in the visible and near-infrared (NIR) region [19], which enables applications working with visible wavelengths. Wild et al. have demonstrated a comparison of one dimensional silver and gold nanowires in terms of plasmon propagation length [29]. They have reported – with both modelling and experimental results – that Ag NWs have longer propagation lengths in NIR wavelengths compared to Au NWs, due to lower optical losses in Ag as compared to Au. Therefore, 1D Ag NWs are generally preferred for waveguiding applications.

Chemically synthesized Ag NWs have been reported to exhibit a dip in the transmission spectra around 350 nm [31] due to the excitation of localized surface plasmon resonance (LSPR) [32]. Figure 2.7 shows the spectral transmittance of Ag

NW films deposited on glass substrates by spin coating with Ag NW concentrations from 0.25 to 3.5 mg/ml. The dip in transmittance around 350 nm can be seen from the figure. It is also seen that the transmittance decreases with the increased Ag NW solution concentration due to the increased nanowire coverage area.
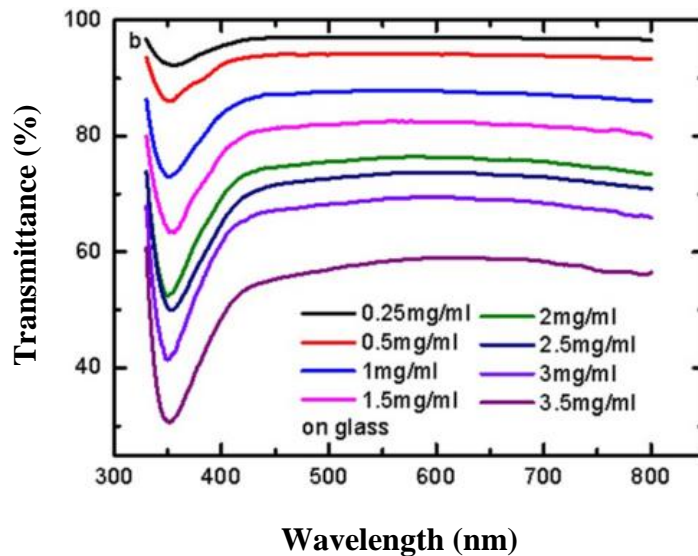
Figure 2.7 Spectral transmittance of Ag NW films prepared on glass by spin coating with Ag NW concentrations from 0.25 to 3.5 mg/ml [31].

2.3.1.1 Polyol Synthesis of 1D Silver Nanowires

1D Ag NWs used in this work were provided from Assoc. Prof. H. Emrah Ünalan's group in Metallurgical and Materials Engineering Department, Middle East Technical University and were synthesized through polyol synthesis.

The polyol synthesis is a liquid-phase synthesis employing high-boiling, multivalent alcohols - so-called polyols - and is directed to synthesis of nanoparticles [33]. The process relies on the reduction of an inorganic salt using a polyol at an elevated temperature. To inhibit agglomeration of the colloidal particles, a surfactant is usually used [34].

In this study, Ag NWs were produced using ethylene glycol (EG) as both solvent and reducing agent, poly(vinylpyrrolidone) (PVP) as stabilizing agent, and silver nitrate (AgNO$_3$) as Ag source. During synthesis, the introduction of Ag$^+$ ions into the solution induces Ag nanoparticle (Ag NP) formation via homogeneous nucleation. The Ag NPs remain at the nanoscale due to the chemical adsorption of PVP molecules onto the

surfaces of as-formed Ag NPs. As the reactions proceed, some Ag NPs begin to dissolve and grow into larger nanoparticles. Moreover, some nanoparticles can grow into multitwin particles with the passivation of some facets of these particles by PVP. As the reactions proceed, PVP passivates (100) faces of these multitwin particles, leaving (111) planes active. The mechanism behind this is that the chemical bonding between PVP and (100) plane is stronger to that between PVP and (111), which results in anisotropic growth at [110] direction. As the introduction of Ag^+ ions into the solution continues, multitwin particles grow into 1D Ag NWs [34], [35].
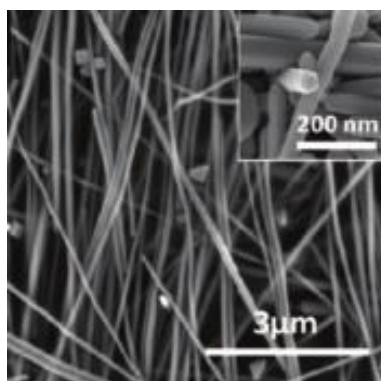
Figure 2.8 SEM image of Ag nanowires. The pentagonal cross section of the nanowires is shown in the inset [34].

As it is reported by Coskun et al. in Ref. [34], self-seeding polyol synthesis of Ag NWs with optimum process conditions results in pure, crystalline Ag NWs with pentagonal cross sections. The SEM image of Ag NWs is seen in Figure 2.8. It is seen from the SEM image that the nanowires have high aspect ratio.

2.3.3 Coaxial Nanowires

Coaxial nanowires can be defined as 1D nanocomposites with different components, combining the advantages of core and tube units. As it is illustrated in Figure 2.9, in coaxial nanowires there is a spacer layer between the core and the tube which produces more complex hybridized resonances. The tunable resonances arise from the interaction and mixing of the wire and capillary plasmons. The strength of the interaction between these two types of plasmons is governed by the thickness of the components of the coaxial nanowire. A thin nanowire results in strong plasmon

mixing, whereas a thick nanowire isolates the plasmons of the two surfaces. The transmission spectra of the coaxial nanowires depend strongly on the inner radii, the separation distance (i.e. thickness of the spacer layer) and the number of the tube layers [36].
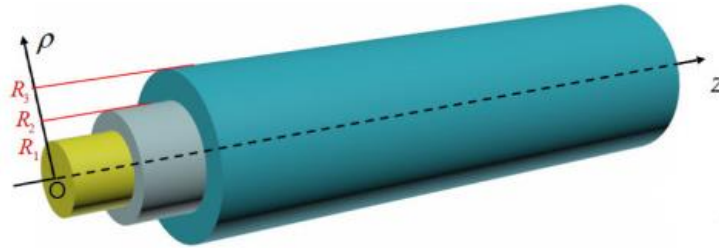
Figure 2.9 Schematic of coaxial nanowire consisting of core, spacer, and tube layers with radius of R_1, R_2, and R_3, respectively.

Xu et al. have demonstrated that the transmission characteristics of a coaxial nanowire can be tuned by changing the thickness and the dielectric constant of the spacer layer [36]. When they decreased the separation and increased the dielectric constant simultaneously, the transmission band was found to be widened, which enhances transmission.

An amenable structure to obtain sub-wavelength confinement are metal/insulator/metal (MIM) waveguides, where the plasmon mode is confined inside the dielectric layer. It has been demonstrated that even when the thickness of the spacer layer is decreased, an appreciable fraction of the total mode energy locates inside the metal. However, increased localization to the interface leads to a high electric field inside the dielectric, pushing the effective mode length of the one-dimensional system into the deep sub-wavelength region. As a result, the mode is confined below the diffraction limit inside the MIM structure [17].

2.3.4 Titanium Dioxide as the Dielectric Layer

Being a wide band gap [37], [38], high refractive index [39] and high dielectric constant (κ) [40] material, titanium dioxide (titania, TiO_2) is of great interest in applications requiring high-κ oxides. Due to its chemically resistant and non-toxic nature TiO_2 has been used in various applications such as pigments [41], sunscreen creams [42], paints [43], toothpastes [44] and so on since the early twentieth century.

In 1972, Honda and Fujishima discovered the electrochemical photolysis of water on a TiO_2 electrode under ultraviolet (UV) light [45]. Since then, great efforts have been made to the research of TiO_2 material, from photovoltaics and photocatalysis to photoelectrochemical cells [46]–[48].

2.3.4.1 Crystal Structure

TiO_2 has three main crystal structures: anatase, rutile and brookite. Among them, brookite is rarer and requires a difficult preparation process. Therefore, anatase and rutile are the most common crystal structures from the application perspective.

The basic building block of anatase and rutile is a distorted TiO_6 octahedron where the degree of distortion is higher in anatase. Therefore, there are differences in the stacking arrangements in anatase and rutile even though their binding geometries are very similar. As a result, the crystal faces with the lowest energy are (101) and (001) for anatase and (110) and (100) for rutile. These crystal faces are thus the most common for polycrystalline samples [49]. Ball-and-stick models of anatase (101) and rutile (110) can be seen in Figure 2.10.
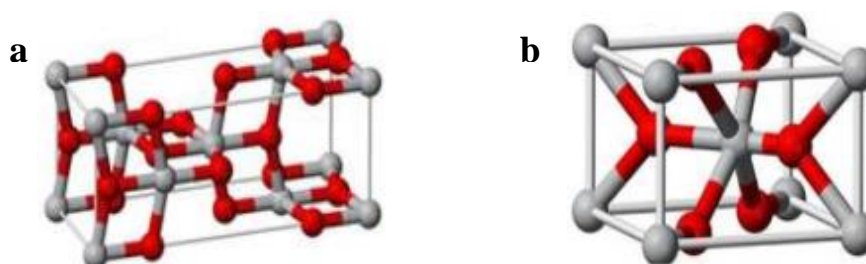
Figure 2.10 Ball-and-stick models of different titania surfaces. (a) Anatase TiO_2 (101), and (b) rutile TiO_2 (110). Red ball: O; grey ball: Ti.

2.3.4.2 Electrical and Optical Properties

TiO_2 is an n-type semiconductor with band gaps of 3.4, 3.20 and 3.03 eV for amorphous, anatase, and rutile TiO_2, respectively [50]. The conductivity of TiO_2 depends on the oxygen deficiencies within the structure through creation of defects such as oxygen vacancies, Ti^{3+} and Ti^{4+} interstitials. Especially in vacuum systems, oxygen deficiency is easily created in TiO_2. Post production heat treatment in oxygen rich or reducing atmospheres is usually performed to tailor the amount of oxygen

deficiency and thus the conductivity. Impurities are also effective on the electrical properties of TiO_2. For example, hydrogen impurities inside the TiO_2 material can increase the electrical conductivity [51].

TiO_2 is a high dielectric constant (high-κ) material. The κ values are 18 for amorphous, 40 for anatase, and 86-170 for rutile depending on its crystal orientation [52], [53]. As a high-κ dielectric, TiO_2 has been utilized as an alternative gate oxide in metal-oxide-semiconductor field-effect transistors (MOSFETs) and as trench capacitor in dynamic random access memory (DRAM) devices [54]. The biggest limitation in these applications for the use of TiO_2 is the high leakage due to its relatively small band gap and n-type conductivity. Oxygen deficiencies also facilitate the increased conductivity. As its band gap energy indicates, TiO_2 is transparent to visible wavelengths. Also, TiO_2 has the highest refractive index among all oxides [53].

CHAPTER 3

ATOMIC LAYER DEPOSITION

3.1 General Background

Atomic Layer Deposition (ALD) has been developed as a chemical gas phase thin film growth technique based on sequential surface reactions [55]. Along with being a variant of the Chemical Vapor Deposition (CVD) technique, ALD has some unique properties making it differ from the other chemical vapor deposition techniques. CVD is mostly used to grow solid thin films on heated substrate surfaces. In this technique, a mixture of precursor gases is flown into the chamber for rapid surface reactions. For high deposition rates, the substrate surface has to be sufficiently hot, that is, the process is typically carried out at temperatures ranging from 200 to $1600^{\circ}C$. Ideally, there should not be any homogeneous gas-phase reactions between the precursors, which would yield particulate formation during the thin film growth [56]–[58]. In ALD process, on the other hand, the reactive precursor gases are exposed to the substrate surface separately, one at a time, and the ALD chamber is pulsed with an inert carrier gas between the precursor pulses. The surface reactions occur sequentially, after each precursor pulse, forming monolayers of the solid thin film. Since the chemisorption of the reactants require active catalytic sites on the surface, the reaction terminates itself once all the catalytic sites are reacted. The ALD process is therefore called self-limiting or self-terminating. The self-limiting nature of ALD provides thickness control at the sub-ångstrom or monolayer level, and induces perfect conformality and step coverage on high aspect ratio structures [59], [60].

3.2 History of ALD

The starting point of the gas-phase layer by layer deposition technique, known as 'Atomic Layer Deposition' (ALD) in the modern community, is controversial [61]. According to most sources, it was developed as "atomic layer epitaxy (ALE)" in the late-1970s by Suntola and his co-workers in Finland [55], [62]. The first experiments were made in 1974 to produce high quality polycrystalline ZnS:Mn and amorphous Al_2O_3 insulator films on large-area substrates for thin-film electroluminescent (TFEL) flat-panel displays [55], [63].

In her review article, Puurunen [61] stated that ALD was originally introduced as 'Molecular Layering' (ML) by Soviet scientists Aleskovskii and Kol'tsov in the 1960s. The idea laying behind molecular layering technique was first proposed by Prof. V. B. Aleskovskii in his Ph.D. thesis dating back to 1952. In his thesis titled 'Matrix Hypothesis and Way of Synthesis of Some Active Solid Compounds', Aleskovskii suggests the matrix (framework) hypothesis aiming a new understanding of transformations of compound solids. According to the hypothesis there are two possible ways for chemical transformations of solids: reorganizing the functional groups on the surface of a solid framework (independent from the core atoms), and substituting the bulk atoms (transformation of the core) [64], [65]. In 1965, Aleskovskii and his research group described the $TiCl_4/H_2O$ and the $GeCl_4/H_2O$ processes to grow TiO_2 and GeO_2, respectively. The Finnish and the Russian groups became aware of each other's work in the late-1980s [61].

3.3 Applications

Thin-film electroluminescent (TFEL) displays is the oldest application of ALD requiring films with high endurance against large electric fields. Providing high dielectric strength, uniformity over large areas, and low pinhole density, the ALD technique has been used successfully in TFEL technology since the early-1980s [57], [66]. In the mid-1980s, the interest was focused on epitaxial growth of III-VI and II-VI compounds, however, because of the complex surface chemistry, no remarkable success was achieved [59].

The emergence of silicon-based microelectronics in the 1990s made ALD more attractive. Shrinkage in device dimensions and high aspect ratio structures in integrated circuits (ICs) required thickness control at atomic level and highly conformal deposits. Among other thin film techniques, ALD provides the highest conformality on high aspect ratio structures [60]. ALD also met the challenging requirements for other applications by enabling the deposition of high quality, high-κ dielectric materials. These high-κ dielectrics are employed as alternative gate oxides in metal-oxide-semiconductor field-effect transistors (MOSFETs) and as trench capacitors in dynamic random access memory (DRAM) devices [54].

Due to thickness control at sub-atomic level and deposition at mild temperatures, ALD is frequently employed in energy storage [67]–[70], microelectromechanical (MEMS) [71], [72] and nanoelectromechanical systems (NEMS) [73], [74], catalysis [75], [76], coating of fibers [77], [78], that is, in almost any field of nanotechnology research. The rising interest towards ALD technique around the world can be seen in Figure 3.1, showing the increasing number of ALD publications per year [79].
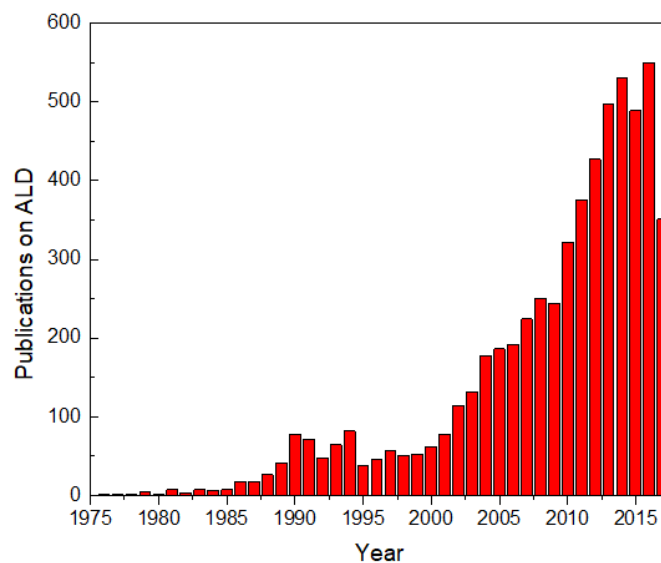
Figure 3.1 The number of scientific publications on ALD per year between 1975 and 2017, analyzed from ISI Web of Science [79].

3.4 ALD Process

3.4.1 Basic Principles

ALD is a thin film technique which relies on sequential gas-solid reactions of two or more precursors, separated by purging or evacuation periods. The reactions are repeated in a cyclic manner and one ALD cycle consists typically of four steps, as illustrated in Figure 3.2:

1.   Exposure of the first precursor (Reactant A)

2.   Purge or evacuation to remove excess precursor molecules and gaseous by-products

3.   Exposure of the second precursor (Reactant B)

4.   Further purge or evacuation to remove excess precursor molecules and gaseous by-products.
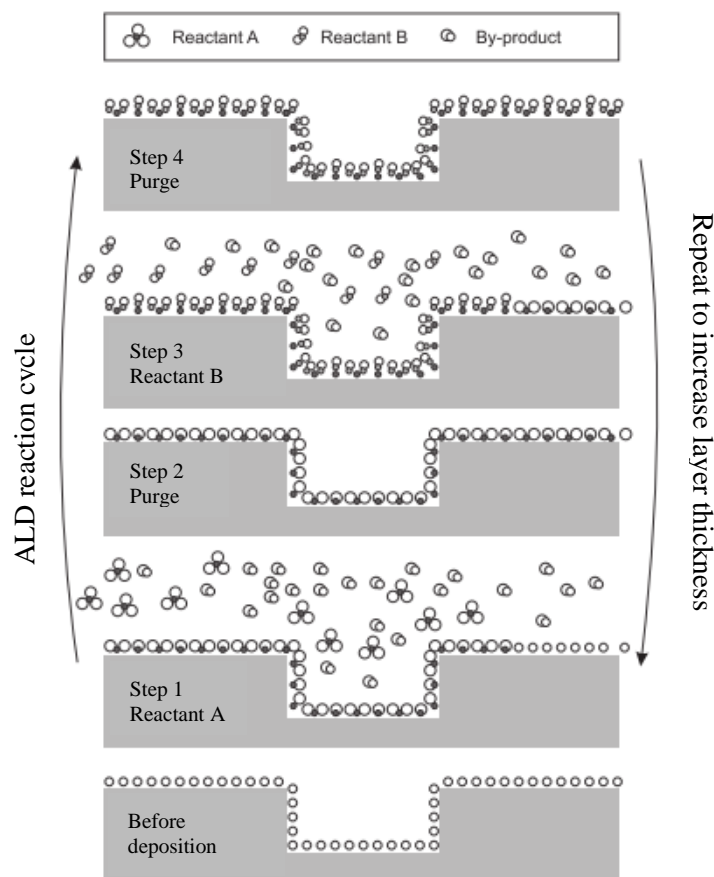
Figure 3.2 Schematic illustration of one ALD growth cycle.

In a typical ALD process, the precursor molecules do not tend to react with each other, and hence the chemisorption (steps 1 and 3) terminates once all the active catalytic sites are occupied. This behavior results in a self-limiting growth mechanism – the same amount of material is deposited in each cycle – which is known as the *growth per cycle* (GPC). The growth cycles are repeated according to the desired film thickness.

Although some surface sites will react before other surface sites because of different precursor fluxes, the precursor molecules will adsorb and then desorb from these occupied sites, and will subsequently react with other unreacted surface sites. Therefore the resultant thin film will be quite conformal to the original substrate. The self-limiting nature of ALD provides a non-statistical deposition by removing the effect of random precursor flux. Since no surface sites are left unreacted, the films tend to be very continuous and pinhole-free. Above mentioned *irreversible* and *saturating* reactions in ALD process induce uniform thin film deposition on large-area substrates and complex 3D shapes [60], [61], [80]. Figure 3.3 illustrates the comparison of irreversible and saturating gas-solid reactions to other types of adsorption.
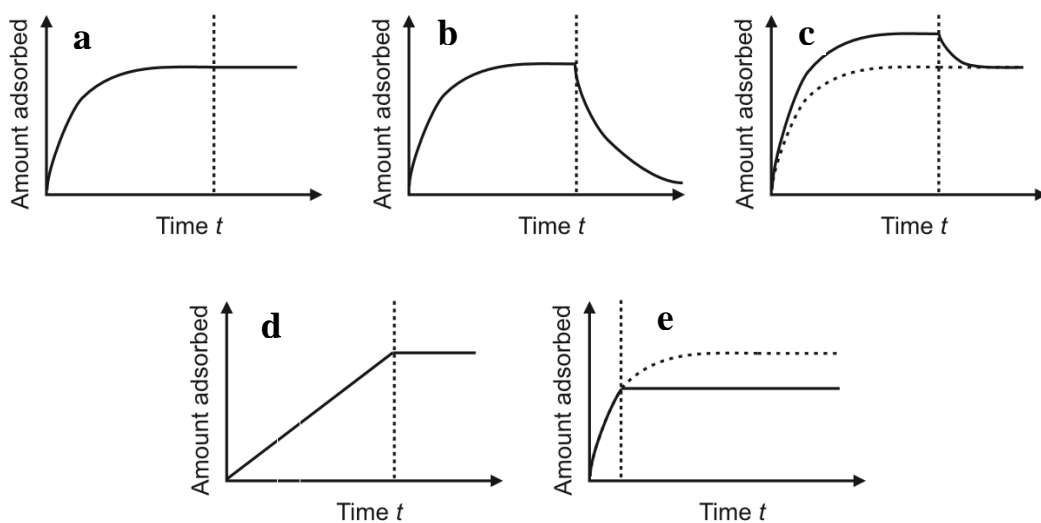
Figure 3.3 Schematic illustration of various types of adsorption: (a) irreversible saturating adsorption (as expected for ALD), (b) reversible saturating adsorption, (c) combined irreversible and reversible saturating adsorption, (d) irreversible non-saturating adsorption (i.e. deposition), and (e) irreversible saturating adsorption not allowed to saturate. The dashed vertical line denotes the end of reactant pulse (Step 1 or 3) and the beginning of purge sequence (Step 2 or 4), as described in the text [80].

The temperature range, in which the ideal self-limiting ALD behavior is satisfied, is known as the *ALD window*. The ideal ALD growth may not be achieved in all ALD systems. Some ALD systems may not satisfy the self-terminating reactions since the surface species may decompose, allowing additional adsorption. On the other hand, in some ALD systems, the surface reactions may never reach hundred percent completion. They may continue until some percentage of completion and then terminate. Although these reactions will show self-limiting growth, they will leave large amounts of impurities in the films [60]. The ideal ALD behavior between the non-ideal ALD regions is shown in Figure 3.4.
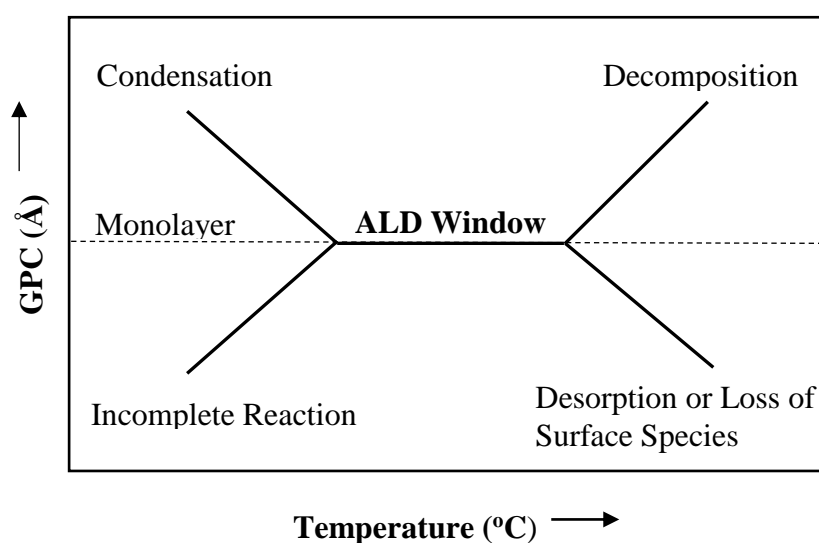
Figure 3.4 GPC as a function of temperature showing the ALD window.

At very high temperatures, the first precursor may decompose on the surface before having time to react with the second precursor. The growth rate would then be higher than it is expected for a typical ALD process. If the first precursor does not decompose, it may still desorb from the surface before reacting with the second precursor. In this case the growth rate would be less than expected. This case is more likely if the first precursor is physisorbed rather being chemisorbed. On the contrary, if the temperature is too low, more than one monolayer may be adsorbed during one cycle or even condensation on the surface may occur. It would reduce the growth rate.

Alternately, the reaction rate may be too slow at low temperatures that the reaction may need too much time to achieve completion. In this circumstance one cycle may

take hours rather than seconds, and thus there may not be enough time for a monolayer to reach completion [56].

It should further be noted that GPC does not need to be constant, even in the ALD window. GPC is a function of three parameters: the reactants, the surface where the reactions take place, and the processing temperature [81]. The effect of temperature on the growth behavior is explained above. The surface effects the saturation of a monolayer by two means: *steric hindrance of the ligand*s and *the number of reactive sites*. Due to the steric hindrance, growth of a full monolayer per cycle should not be expected when compounds (ML_n, where M is metal and L is ligand) are used as precursors. In this case, the ligands of the chemisorbed ML_z species can shield part of the surface from being accessible to the ML_n reactant. The surface is then considered "full".
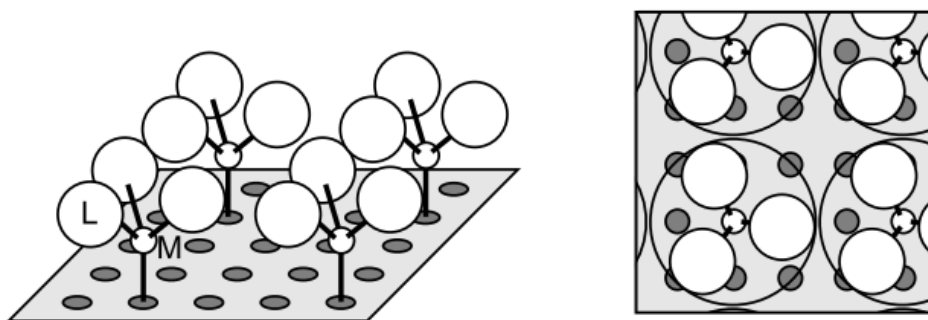
Figure 3.5 Sterically hindered chemisorption on the basis of the size and geometry on the chemisorbed ML_z species [82].

A model for the analysis of sterically hindered chemisorption by Ylilammi et al. [82] is seen in Figure 3.5. The effect of the original substrate on the GPC is only seen in the beginning of the growth and is lost with increasing extent of the deposition. This is also the reason for different growth behaviors with the varying number of cycles (Figure 3.6). The number of reactive sites on the surface may also be less than required to achieve the maximum ligand coverage. That is, although space remains on the surface, no bonding sites are accessible [61].
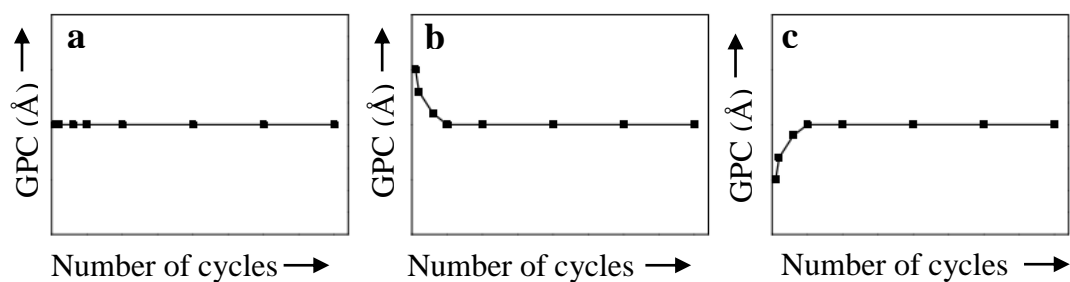
Figure 3.6 Dependency of GPC on the number of ALD cycles reveals different types of growth behavior: (a) linear, (b) substrate-enhanced, and (c) substrate-inhibited.

ALD systems can either be thermal or plasma/radical enhanced. Thermal ALD (T-ALD) systems rely on thermal energy and can be conducted without the plasma or radical assistance. Thermal ALD process may be direct or may be based on compounds. In earlier studies the substrate surface was subjected to atomic species rather than compounds, which is known as direct ALD process. In this process the growth temperature must be maintained high enough to prevent condensation of the first precursor, and the monolayer must be stable. Suntola mentioned the drawbacks of using compounds in his early patent [55]. He stated that due to the decomposition of the compound into its elements, it was extremely difficult to control the stoichiometry, the nucleation properties, and the crystal structure of the deposited film. Later on, he suggested that the same process could be performed using chemical compounds instead of elemental species [63]. The recipe is to find a CVD process using binary reactants and adapt it to ALD process, by separating the exposure of the precursors. The chemistries of thermal ALD processes have negative heats of reaction (see equations below) and the reactions occur spontaneously (i.e. having negative Gibbs free energy change, ΔG) at various temperatures.

$$TiO_2 \text{ ALD:} \quad TiCl_4 + 2H_2O \longrightarrow TiO_2 + 4HCl \qquad \Delta H = \text{-16 kcal}$$

$$ZnO \text{ ALD:} \quad Zn(CH_2CH_3)_2 + H_2O \longrightarrow ZnO + 2C_2H_6 \qquad \Delta H = \text{-70 kcal}$$

The most common materials deposited by thermal ALD systems are binary metal oxides such as TiO_2, Al_2O_3, ZnO, HfO_2, ZrO_2, and Ta_2O_5. Binary metal nitrides such as TiN, TaN, and W_2N are also frequently deposited using thermal ALD systems [60].

28

Sulfides (e.g., ZnS,CdS) and phosphides (e.g., GaP, InP) can also be grown by thermal ALD [60].

Deposition of single-element materials (i.e. metals, semiconductors) are very challenging by thermal ALD systems. However, with the aid of plasma or radicals, this challenge can be overcome [83]. The radicals or other energetic species in the plasma make the reactants highly reactive and thus activate the reactions where the thermal energy alone becomes insufficient. Plasma-enhanced ALD (P-ALD) is known to exhibit better material properties when compared to thermal ALD, however, conformality of the films may not be satisfying due to radical recombination. Plasma-induced damage may also occur in the case of direct plasma [84], [85].

An overview of materials deposited by ALD can be seen in Figure 3.7 [61].
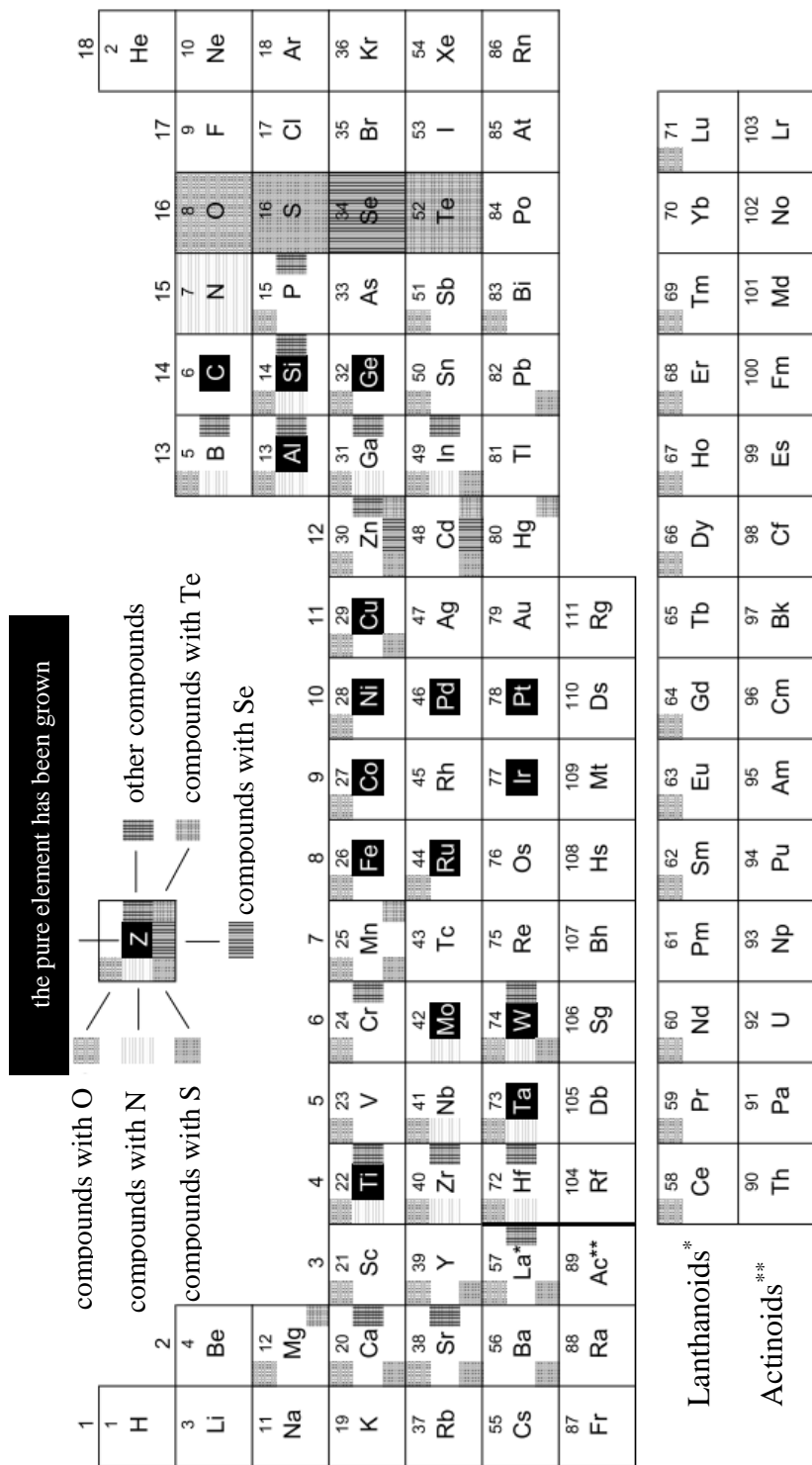
Figure 3.7 Overview of the materials grown by ALD [61].

3.4.2 Requirements for Precursors

In ALD process a variety of inorganic and metalorganic precursors are employed. The five most commonly referred requirements can be listed as volatility, stability against self-decomposition, reactivity, availability, and inertness of its by-products [57], [61].

- *Volatility* – An ALD reactant must be volatile either at room temperature or at elevated temperatures. The minimum and the desired vapor pressure values is generally 0.1 and 1 Torr, respectively. However, the optimum value is reactor specific.

- *Stability against self-decomposition* – The self-limiting growth is not achievable unless the selected precursor is stable at the ALD operating temperature. The self-decomposition of the precursor during its reaction with the substrate surface or the growing film will result in a CVD-like growth.

- *Reactivity* – In ALD the precursors do not meet at the gas phase due to the alternate pulsing, that is, there are no gas phase reactions. Therefore, most aggressively reacting precursors must be selected to ensure rapid completion of the reactions and thus short cycle times and effective precursor usage. This means the reactions must have as negative a Gibbs free energy change, ΔG, as possible.

- *Availabality* – The precursors should be synthesized or supplied easily in sufficient quantities.

- *Unreactive by-products* – It is preferable that the selected precursors produce unreactive volatile by-products which can easily be purged out from the ALD system. Reactive by-products may cause corrosion problems in the reactor and also may readsorb on the film surface, blocking adsorption sites from the precursor molecules. In the worst scenario they may etch the growing film.

Impurity of the precursors and residual contaminates (e.g., Cl, C, N, H) may become an important concern for especially semiconducting materials as they are more sensitive to impurities and contaminants. Low cost, non-toxicity, environmental friendliness are among other requirements.

3.4.3 Benefits and Limitations

The self-limiting growth mechanism of ALD offers unique benefits including precise thickness control at subatomic level, excellent conformality and uniformity on large area or complex shaped substrates (Figure 3.8), stoichiometry control and reproducibility. Characteristic features of ALD with consequent advantages are summarized by Ritala and Leskelä are given in Table 3.1 [57].
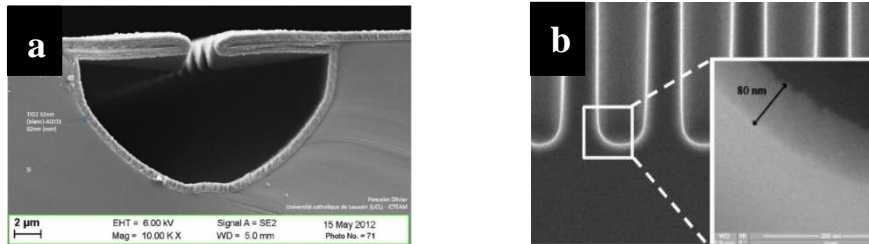
Figure 3.8 SEM images of ALD materials. (a) ALD TiO_2 and Al_2O_3 multilayers on Si substrate [86], and (b)80 nm ALD thick Al_2O_3 film in 2.5μm wide trenches with an aspect ratio of 10 [87].

Accurate control of material composition enables the deposition of quantum dots and quantum wells [88], [89], nanolaminates and superlattices [90]–[92], and also doped [93], [94], graded [95], and alloy [96] thin films. Precise control of the layer growth makes ALD a powerful method for coating particles [97]–[99], and synthesizing complex nanostructures using templates such as carbon nanotubes [100], nanofibers [101], anodic aluminum oxide membranes [102], etc. The opportunity of low processing temperatures in ALD enables the surface modification of temperature-sensitive organic substrates (polymers [103], self-assembled peptide nanofibers [104], etc.), and even on biological substrates such as tobacco viruses [105], and butterfly wings [106]. Surface engineering and processing of various nanomaterials were reviewed by Knez et al. [107] and Kim et al. [108] reported the utilization of ALD in the aspect of nanomaterials and emerging nanodevices.

The major drawback of ALD is slow grow rates because it takes at best one cycle to deposit a monolayer. However, large-batch capability of ALD together with shrinking device dimensions and thus requirement for thinner films (typically < 200 Å) made this main drawback become less important [57].

Table 3.1 Characteristic features of ALD with the consequent advantages [57].

Characteristic feature of ALD	Inherent implication on film deposition	Practical advantage
Self-limiting growth process	Film thickness is dependent only on the number of deposition cycles	Accurate and simple thickness control
	No need of reactant flux homogeneity	Large-area capability Large-batch capability Excellent conformality No problems with inconstant vaporization rates of solid precursors Good reproducibility Straightforward scale-up
	Atomic level control of material composition	Capability to produce sharp interfaces and superlattices Possibility to interface modification
Separate dosing of reactants	No gas phase reactions	Favors precursors highly reactive toward each other, thus enabling effective material utilization
	Sufficient time is provided to complete each reaction step	High quality materials are obtained at low processing temperatures
Processing temperature windows are often wide	Processing different materials are readily matched	Capability to prepare multilayer structures in a continuous process

3.5 Atomic Layer Deposition of Titanium Dioxide

3.5.1 Selection of Precursors

A variety of inorganic and metalorganic precursors, which are generally classified according to their ligand groups, are used in ALD processes as aforementioned. ALD of TiO_2 has been extensively studied using various precursor combinations (Table 3.2). Of inorganic reactants, halides such as $TiCl_4$, TiI_4, TiF_4; and of metalorganic reactants, alkoxides such as $Ti(OMe)_4$, $Ti(OEt)_4$, $Ti(O^iPr)_4$, and alkylamides such as $Ti(NMe_2)_4$, $Ti(NEt_2)_4$, $Ti(NMeEt)_4$ have been employed as titanium precursors. Water is the most commonly used oxygen source, and other oxygen sources are H_2O_2, O_3 and oxygen radicals.

Table 3.2 Selected precursor combinations used in ALD TiO_2 process.

Titanium precursor	Oxygen source	References
$TiCl_4$	H_2O, H_2O_2, O_3	[109]–[114], [115], [116]
TiI_4	H_2O, H_2O_2, O_2	[117], [118], [119]
TiF_4	H_2O	[120]
$Ti(OMe)_4$	H_2O	[121]
$Ti(OEt)_4$	H_2O	[122], [123], [124]
$Ti(O^iPr)_4$	H_2O, H_2O_2, O_2-radicals, O_3	[124]–[128]
$Ti(NMe_2)_4$	H_2O, H_2O_2, H_2O-plasma, O_2-plasma, O_3	[129], [130]–[138]
$Ti(NEt_2)_4$	H_2O, O_3	[134]
$Ti(NMeEt)_4$	H_2O, O_3	[134]

The common precursor $TiCl_4$ is a liquid reactant forming corrosive by-products HCl and residual $TiCl_4$ when used with H_2O or H_2O_2 as oxidant [109]–[114]. A relatively less corrosive TiI_4 is another precursor used for ALD TiO_2 [117], [118]. Titanium alkoxides have become promising precursors without corrosive halogen by-products. However, studies reveal that the decomposition of these precursors occur even at low processing temperatures [122], [139].

For the selection of precursors one should consider that metal amide compounds are expected to have much higher reactivity with water (or a hydroxylated surface) when compared to metal halide compounds. The reason for low reactivity of metal halide compounds with water is that the bond energy of metal-halide is much stronger than that of the metal-nitrogen bond [129], [130]. Among titanium alkylamides $Ti(NEt_2)_4$ and $Ti(NMeEt)_4$ are reported to start decomposing at temperatures well below 300^oC [134].

In this study, $Ti(NMe_2)_4$ (tetrakis(dimethylamido) titanium, TDMAT) and water were used as the precursors. TDMAT is the most commonly studied ALD titanium alkylamide with a counter reactant H_2O, H_2O_2, H_2O-plasma, O_2-plasma or O_3 as can be seen in Table 3.2. A common feature of all these studies is that the growth per cycle has been found to decrease as the substrate temperature increases (Figure 3.9 (a)). The possible mechanism for this behavior is decribed by Xie et al. [129]. The two half reactions for ALD TiO_2 with TDMAT and H_2O are described as follows:

$$Ti(N(CH)_3)_2)_4 + TiO_2 - OH^* \longrightarrow NH(CH_3)_2 +$$
$$TiO_2 - O - Ti(N(CH_3)_2)_3{}^*,$$
$$TiO_2 - O - Ti(N(CH_3)_2)_3{}^* + 2H_2O \longrightarrow$$
$$TiO_2 - TiO_2 - OH^* + 3(NH(CH_3)_2).$$
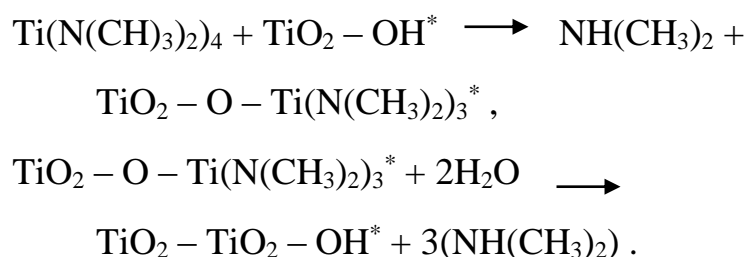
where the asterisks denote the surface species.

They showed by XPS measurements that at low temperatures (i.e. 50^oC) ligand replacement between TDMAT and H_2O happens easily due to the high reactivity between the two precursors and thus the very low energy barrier. Therefore, the growth is high in the low temperature region. As the temperature increases, although the reactivity between the two precursors increases, thermal desorption of the intermediate product become more severe. Since the decomposition temperature of TDMAT was reported as 180^oC [140], Xie et al. assumed that the GPC would be high at temperatures higher than 180^oC due to the non-self-limiting growth [129]. However, the growth rate was still low (Figure 3.9(b)).

a

b
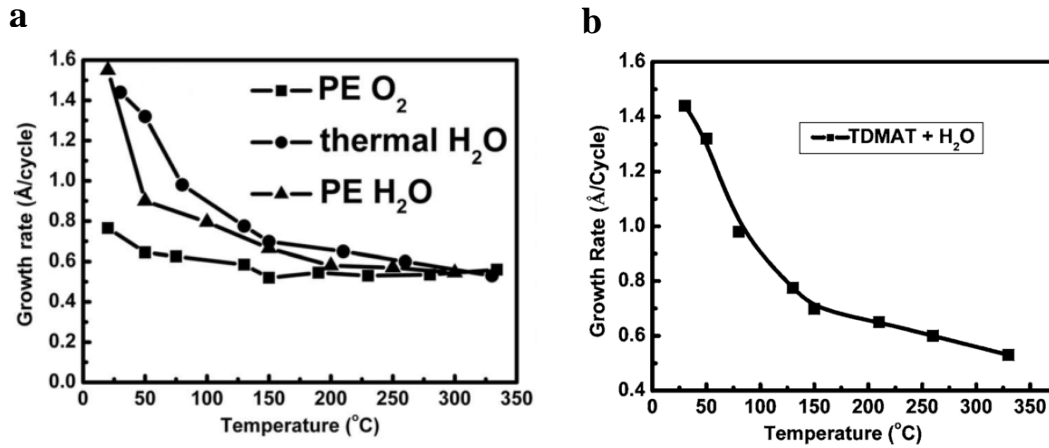
Figure 3.9 Growth rate vs. deposition temperature for TiO_2 grown with (a) TDMAT and different counter reactants [131], and (b) TDMAT and H_2O [129].

3.5.2. Crystallization Behavior

As-deposited ALD materials can be amorphous, polycrystalline, crystalline or contain both amorphous and crystalline phases. The applicability of the ALD films is often dictated by the crystallinity. Crystalline metal oxide films have higher κ-values [80]. On the other hand, amorphous metal oxide films exhibit lower leakage current than polycrystalline films as the grain boundaries act as diffusion pathways [141]. In terms of optical properties, increased surface roughness and grain boundary formation in polycrystalline films induce scattering losses [142]. Generally for crystallinity, a higher growth temperature and thicker film is required. Since thinner films have higher surface to volume ratio, higher energy is required for phase transformation due to the effect of surface energy on phase behavior [80]. In the case for TiO_2, amorphous, anatase, orthorhombic, rutile, and brookite phases have been grown by ALD using various precursor combinations [80], [143]. Crystallinity of TiO_2 films grown by ALD with TDMAT and H_2O or O_2-plasma as counter reactant is given in Table 3.3. As-deposited films are typically amorphous at relatively low temperatures. Post-annealing is commonly performed to obtain crystalline TiO_2 films [144], [145].

Table 3.3 Crystallinity temperatures of ALD TiO_2 films with TDMAT and H_2O/O_2-plasma.

Reactant A	Reactant B	Substrates	Phases		
			Amorphous	Anatase	Rutile
$Ti(NMe_2)_4$	H_2O	Si, H-Si[a], CeO_2, ZnO, Ni	50-250ºC	250-350ºC	300-350ºC
	O_2-plasma	Si, Kapton, SS[a], Zn	50-210ºC	250-400ºC	300-400ºC

[a] H-Si, HF-etched Si; SS, stainless steel.

CHAPTER 4

EXPERIMENTAL METHODS

4.1 ALD Process Optimization

4.1.1 Film Growth

TiO_2 thin films were deposited on 525 µm thick n-type cSi substrates. The n-type cSi substrates were cleaned by standard RCA processing [146] which is succeeded by hydrofluoric acid (10%) treatment to remove the native oxide just prior loading into the ALD chamber.

TiO_2 thin films were deposited using an ALD system (V-Edge YTA-16) operating in thermal mode as can be seen in Figure 4.1. Tetrakis(dimethylamido)titanium (TDMAT) (Sigma-Aldrich) heated at 75 °C and H_2O were used as the sources of titanium and oxygen, respectively. Both precursors were provided in stainless steel cylinders. Nitrogen (N_2) of 5N purity was used as a carrier and purge gas at flow rates of 20 sccm resulting in a working pressure of 0.3 mbar.
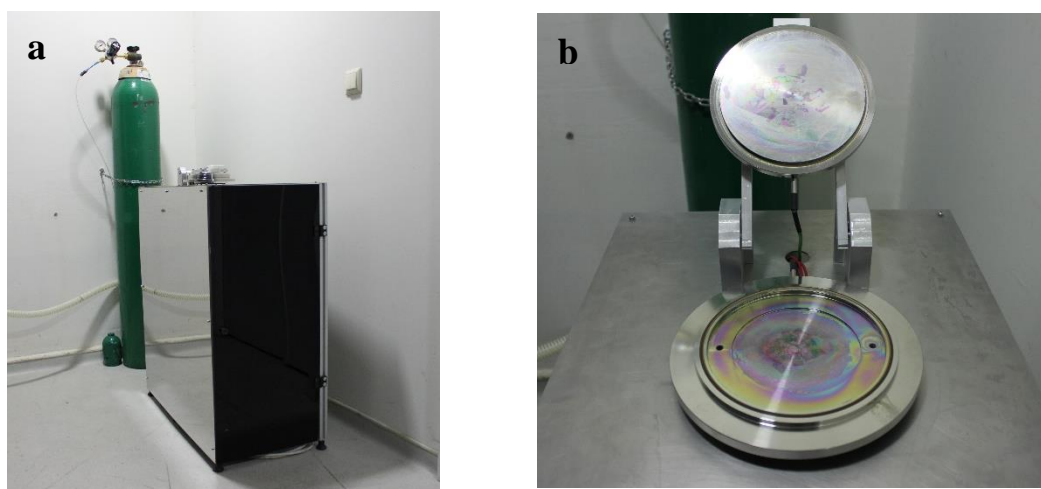
Figure 4.1 (a) The ALD system and (b) the ALD chamber.

During all depositions, each reaction cycle consisted of 0.015 s pulse of TDMAT, 15 s purge with N_2, 0.015 s pulse of H_2O, and 15 s purge with N_2. In this work, ALD TiO_2 thin films were grown for two cases: (i) process temperatures in the range of 50 – 300 °C for a fixed number of cycles 300, and (ii) substrate temperatures 250 °C and 300 °C during 700 reaction cycles. To investigate the effect of post-deposition annealing on crystalline phase formation, the as-deposited amorphous TiO_2 thin films grown at 250 °C during 700 cycles were further annealed at temperatures 300 °C and 350 °C in a flowing N_2 atmosphere for 1 h.

4.1.2   Film Characterization

- Spectroscopic ellipsometry

Films were characterized using spectroscopic ellipsometry (SE) to determine the film thickness and optical properties. The measurements were conducted using a GES-5E model spectroscopic ellipsometer from Semilab Sopra in the spectral range of 1.23-4 eV at an angle of incidence of 70°. The data from the TiO_2 thin films have been fit using the Tauc-Lorentz dispersion model which is applied for amorphous materials as well as transparent conductive oxides [147].

- X-ray photoelectron spectroscopy

Surface components of the films were verified by X-ray photoelectron spectroscopy (XPS) using a PHI 5000 VersaProbe spectrometer with monochromatic $AlK\alpha$ X-ray source. The XPS peak positions were readjusted by taking the C-C bond signal with a C 1s binding energy of 285 eV as reference [148]. The concentration of the surface components were evaluated by integrating the peak area, after subtracting a Shirley-type background and the oxygen content coming from atmospheric hydrocarbons with the aid of XPS Peak 4.1 software.

- Atomic force microscopy

Morphological layouts and average surface roughness were obtained by atomic force microscopy (AFM) using a Veeco MultiMode V system in tapping mode. Data was collected from a surface area of 2×2 μm^2.

- Grazing incidence X-ray diffraction

For the identification of crystalline phases in TiO_2 thin films, grazing incidence X-ray diffraction (GIXRD) was performed under an angle of incidence of 0.3°. This angle is close to the optimum values to analyze anatase and rutile films as it reduces reflections coming from the cSi substrate [115]. The GIXRD patterns were obtained at room temperature in a Rigaku Ultima IV goniometer (CuK_α radiation 1.5418 Å) at 2θ from 20° to 80° with a scanning speed of 2°/min.

- Crystallite size calculation

Average crystallite sizes of TiO_2 thin films were calculated from the broadening of GIXRD reflections by applying refinement through the Rietveld Method (RM). The diffraction patterns were refined with the assistance of GSAS/EXPGUI software. The instrument broadening was refined initially by measuring LaB_6 as the standard reference material. The relation between average crystallite size and GSAS terms is

$$D_{avg} = 18000 \, K \, \lambda / \pi \, LX \qquad (4.1)$$

where K is the Scherrer constant, λ is the incident wavelength (1.5418 Å for CuKα radiation), and LX is the Lorentzian crystallite size coefficient which is determined by the fitting procedure [149]. The K value is taken as 1 for spherical crystals with cubic symmetry [150].

4.2 Coaxial Nanowires

4.2.1 Production Steps

- Substrate cleaning

Polyol synthesized silver nanowires [34] were dropcasted on cSi or glass substrates using a micropipette. cSi substrates were cleaned by standard RCA processing [146] and hydrofluoric acid (10%) treatment as mentioned in subsection 4.1.1. Glass substrates were cleaned by three solvent cleaning which consists of dipping into deionized water, ultrasonic agitation in acetone for 10 min, and dipping into iso-propanol for 5 min, respectively.

- Annealing of silver nanowires

As a result of the polyol synthesis of Ag nanowires, the stabilizing agent PVP presents as a thin film around Ag nanowires. Therefore, this PVP layer needs to be removed before making any deposition on Ag nanowires. To remove the PVP, Ag nanowires on cSi and glass substrates were annealed at 200 °C for 1 h in a flowing N_2 atmosphere.

- Atomic layer deposition of TiO_2 or Al_2O_3

Annealed Ag nanowires on cSi and glass substrates were placed into the ALD chamber. Before the TiO_2 deposition process was initiated, glass substrates were kept at the deposition temperature inside the ALD chamber for 10 min. The deposition process was carried out at a substrate temperature of 150 °C with the same operating conditions that are described in subsection 4.1.1. Three sets of deposition were conducted in order to obtain 10, 15 and 20 nm thick TiO_2 films.

To produce coaxial nanowires with Al_2O_3 spacer layer, annealed Ag nanowires on glass substrates were placed into the ALD chamber and kept at the deposition temperature for 10 min. The aluminum and oxygen precursors were trimethylaluminum (TMA) and H_2O, respectively. The deposition process was carried out at a substrate temperature of 150 °C and with the process cycle consisting of 0.015 s pulse of TMA, 5 s purge with N_2, 0.015 s pulse of H_2O, and 5 s purge with N_2. Three sets of deposition were conducted in order to obtain 20, 35 and 50 nm thick Al_2O_3 films.

- Silver deposition

TiO_2 or Al_2O_3 coated silver nanowires were deposited with a ~5 nm thick silver layer in thermal evaporation system.

4.2.2   Characterization of Coaxial Nanowires

Scanning electron microscopy (SEM) (Nova NanoSEM 430) operating in immersion mode was used to image bare Ag nanowires, TiO_2 deposited Ag nanowires, and coaxial nanowires.

Reflectance and transmittance measurements were performed on bare Ag nanowires, TiO_2 deposited Ag nanowires, and coaxial nanowires - all prepared on glass substrates - using a reflection - transmission setup as can be seen from Figure 4.2.
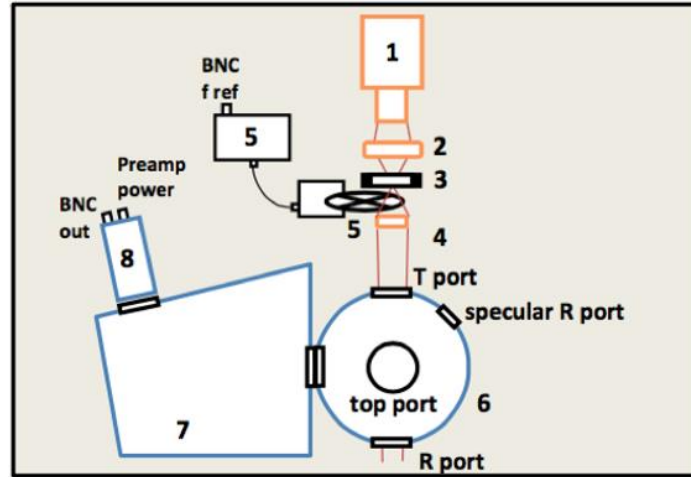
Figure 4.2 Schematic of reflectance – transmittance measurement setup.

The reflectance – transmittance setup includes the following: Halogen lamp, chopper and controller, focusing lens, integrating sphere, lock-in amplifier, monochromator, calibrated silicon detector, and computer. During reflectance and transmittance measurements, the power of the halogen lamp was set to 230 W.

Prior to the reflectance measurements of the TiO_2 thin films, a $BaSO_4$ calibration disk was located at the reflection port of the integrating sphere. The calibration disk is supposed to give 100 % reflectance to be used as the reference data. However, the measured reflectance from the $BaSO_4$ is below 100 %. Later on, the transmission and reflection ports were left empty to measure zero reflection. This step is called "dark" measurement.

After the reference, dark and TiO_2 thin film reflectance measurements, the following equation is used to obtain the total reflectance:

$$R_{total} = \frac{R - Dark}{\dfrac{R_{ref}}{R_{BaSO_4}} - Dark} \qquad (4.2)$$

To measure transmittance, the sample is placed at the transmission port of the integrating sphere with the BaSO$_4$ calibration disk placed at reflection port. The total transmittance is obtain using the following equation:

$$T_{total} = \frac{T}{T_{ref}}$$

(4.3)

CHAPTER 5

RESULTS AND DISCUSSION

5.1 ALD Process Optimization

5.1.1 Effect of Deposition Parameters

Structural, morphological, optical, and electrical properties of atomic layer deposited TiO_2 were extensively investigated by considering the influence of substrate (deposition) temperature and number of process cycles as ALD process parameters. Post deposition annealing was performed on some TiO_2 films to examine the effect of annealing on crystallization behavior and morphology of TiO_2 thin films.

5.1.1.1 Growth Rate

Effect of process temperature on the growth rate in the temperature range between 50 °C and 300 °C was investigated in order to determine a self-limiting growth regime. Films were grown for 300 cycles. The film growth per cycle (GPC) was calculated by dividing the film thickness measured by SE with the number of ALD cycles. In SE measurements, the root mean squared error (RMSE) from the fitting procedure were all in the range of 0.006 to 0.01, fitting very well to the Tauc-Lorentz model.

Figure 5.1 shows the GPC values of ALD TiO_2 thin films as a function of deposition temperature. It can be seen that as the deposition temperature increases, the GPC decreases. This behavior has been demonstrated by several research groups for TiO_2 thin films deposited using TDMAT and H_2O [130], [131], [138], [139]. Xie et al. showed that at lower deposition temperatures, the readily oxidized TDMAT adsorbate surface induces an easy ligand replacement between the two precursors resulting in higher growth rates [24]. At higher growth temperatures, desorption of the intermediate product becomes dominant despite the increasing reactivity between

TDMAT and H_2O. Moreover, George has attributed the higher growth rates at lower temperatures in a typical ALD process to the fact that the reactants could condense on the surface at low deposition temperatures [60]. Decrease in the amount of active catalytic sites present on the surface with increasing process temperature may also decelerate the surface reactions [81].
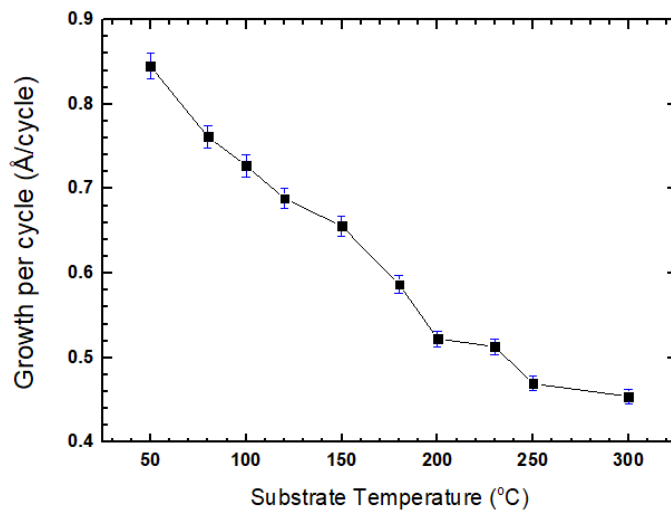
Figure 5.1 GPC of the ALD TiO_2 thin films deposited for 300 cycles at substrate temperatures varying between 50 - 300 °C.

Although the growth per cycle exhibits a constantly decreasing trend, there may still be an ALD window; the temperature range in which the ideal self-limiting ALD behavior is satisfied. Lim et al. have reported a narrow ALD window between 120 °C and 150 °C with a GPC of ~ 0.39 Å/cycle for the TDMAT - H_2O process [130]. Similarly, a rather gradual decline in GPC is seen between 100 °C and 150 °C in Figure 5.1. Therefore, TiO_2 thin film deposition between 80 °C and 180 °C was considered to reveal the existence of the ALD window. As can be seen from Figure 5.2, a saturated growth regime was observed at the growth temperature between 130 °C and 150 °C, with a stable self-limiting growth rate of 0.65 Å/cycle.
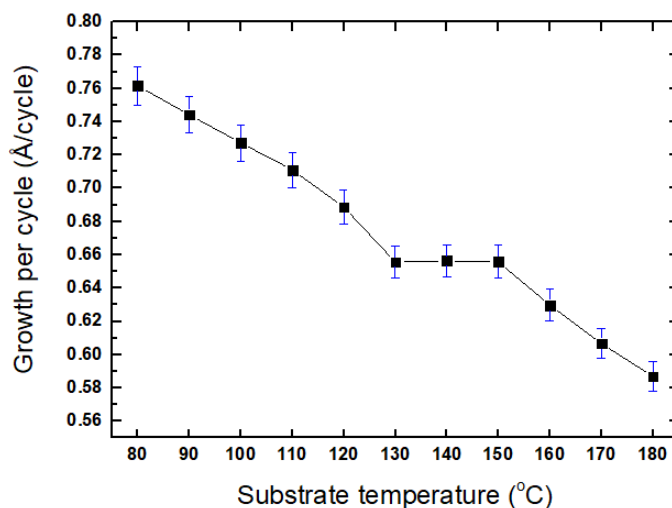
Figure 5.2 GPC of the ALD TiO$_2$ thin films deposited for 300 cycles at substrate temperatures 80 - 180 °C showing the narrow ALD window between 130 °C and 150 °C.

5.1.1.2 Composition

Quantitative XPS analysis was performed to determine the composition of the as-deposited TiO$_2$ thin films grown at temperatures ranging between 50 and 300 °C for 300 cycles. It has been stated by Puurunen that impurities of nitrogen, carbon, and hydrogen are often found in the films for the use of alkylamide precursors such as TDMAT [61]. As was expected, nitrogen was detected in TiO$_2$ thin films deposited at temperatures varying from 50 to 150 °C. As the substrate temperature was increased, nitrogen content was found to decrease (i.e. 2.3 % for 50 °C, 2.1 % for 80 °C and 100 °C, and 1.4 % for 150 °C). At higher growth temperatures no N signal was observed.

Along with nitrogen content at lower deposition temperatures, high carbon content was observed for all growth temperatures, which is thought to arise from the organic carbon contamination at the film surface due to adventitious carbon. Survey spectra of the film deposited at 150 °C before and after sputtering are presented in Figure 5.3. Surface contaminations such as carbon and nitrogen appearing in Figure 5.3(a) were removed by sputtering as shown in Figure 5.3(b) to better quantify the thin film composition.

47
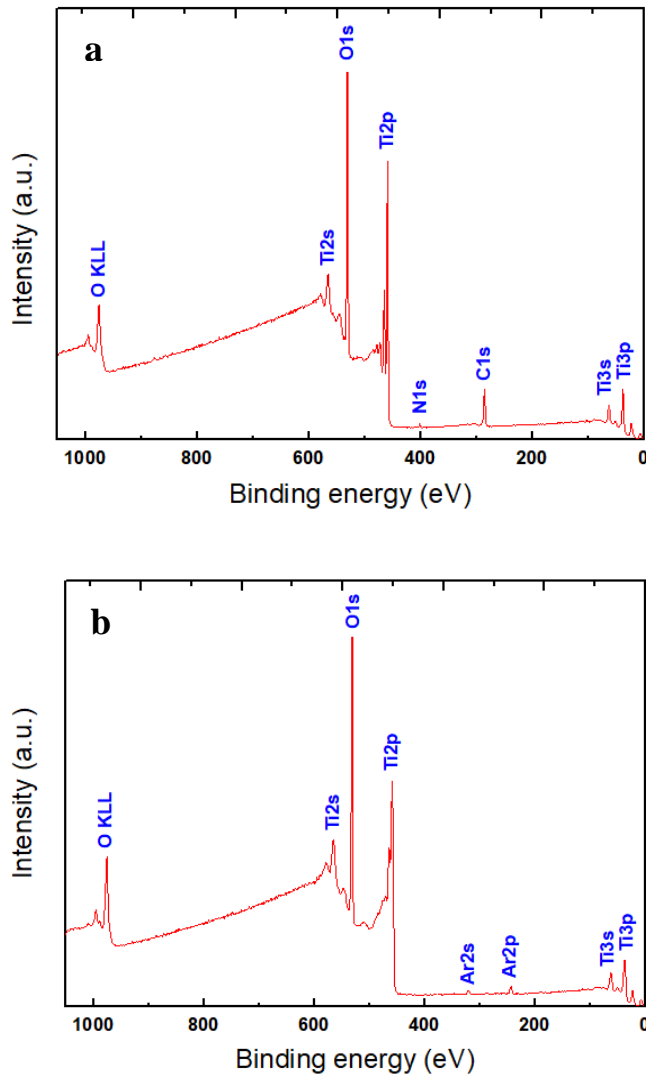
Figure 5.3 XPS survey spectra of the ALD TiO_2 thin films deposited at 150°C for 300 cycles (a) before and (b) after sputtering with argon.

Figure 5.4 demonstrates the Ti2p and O1s XPS spectra of the non-sputtered TiO_2 thin film grown at 150 °C. Stoichiometry of this film was calculated to be $TiO_{1.73}$ using the deconvoluted peak areas and the relative sensitivity factors [151]. For comparison with the calculated film stoichiometry, a second measurement was performed on the TiO_2 thin film deposited at 150 ºC, which was exposed to in-situ argon sputtering to clean the surface from carbon and nitrogen content. The sputtered film had an O/Ti ratio of 1.70 which is in good agreement with the calculated value. Thus, the deconvolution method was further employed to calculate the stoichiometry of the non-sputtered TiO_2 thin films deposited at other deposition temperatures.
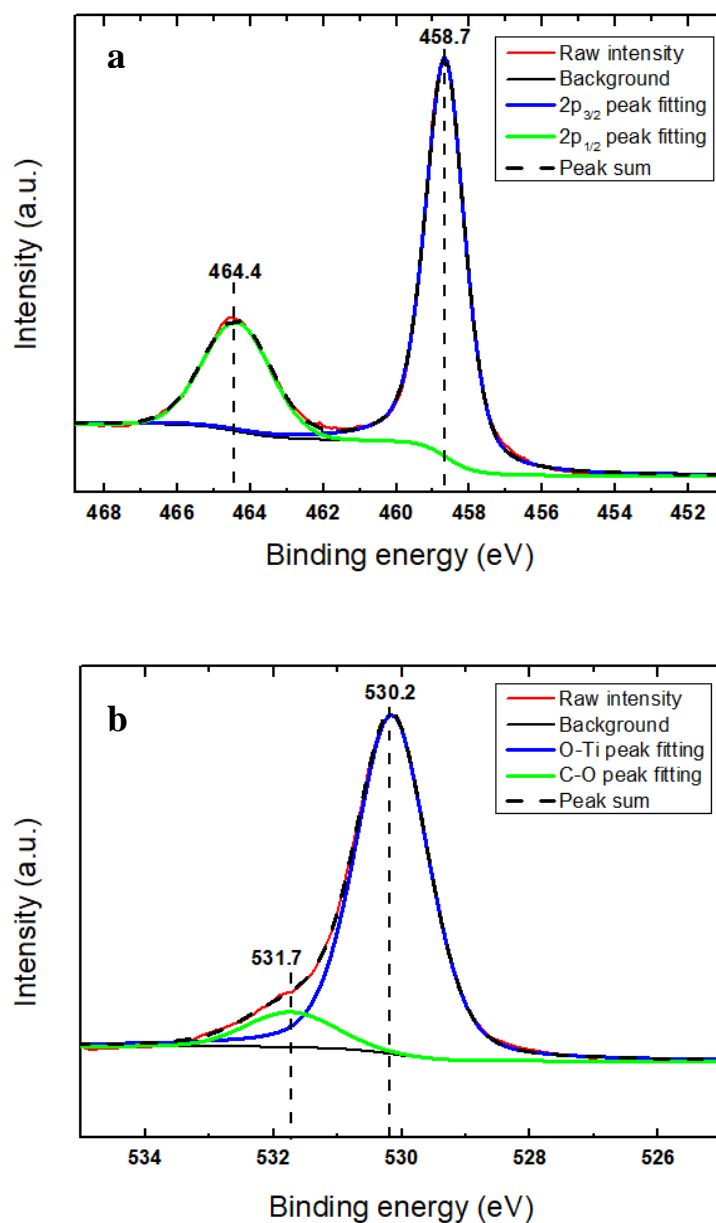
Figure 5.4 High resolution XPS spectra of the (a) Ti2p and (b) O1s peaks of the TiO_2 thin film deposited at 150 °C for 300 cycles.

Figure 5.5 demonstrates the stoichiometry of the TiO_2 thin films after the deconvolution of the oxygen peaks from the carbon containing species. The lower O/Ti ratio at lower temperatures may be attributed to the high film growth rate in this region. It is worth mentioning that for all as-deposited films, the $Ti2p_{3/2}$ and $Ti2p_{1/2}$ peak separation value (i.e. 5.7-5.8 eV) are in good agreement with the literature data indicating the existence of stoichiometric TiO_2 [152], [153]. However, the films are oxygen deficient in fact because they are produced in a vacuum system (see subsection 2.3.4.2).
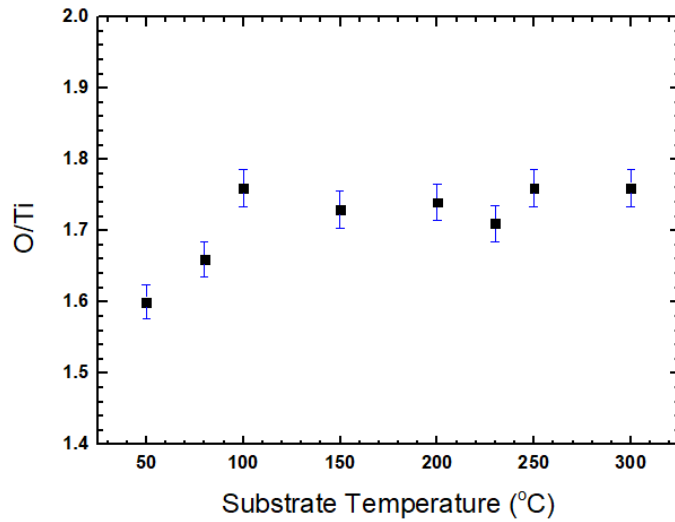
Figure 5.5 O/Ti atomic ratio of the TiO_2 thin films as a function of deposition temperature.

5.1.1.3 Microstructure

Figure 5.6 shows the GIXRD data of TiO_2 thin films deposited at substrate temperatures from 50 °C to 300 °C for 300 reaction cycles. TiO_2 films deposited at temperatures lower than 300 °C give no diffraction peak except for substrate-related reflections marked by asterisk, revealing amorphous nature of these films. For the film grown at 300 °C, diffraction peaks of anatase phase was observed [154].
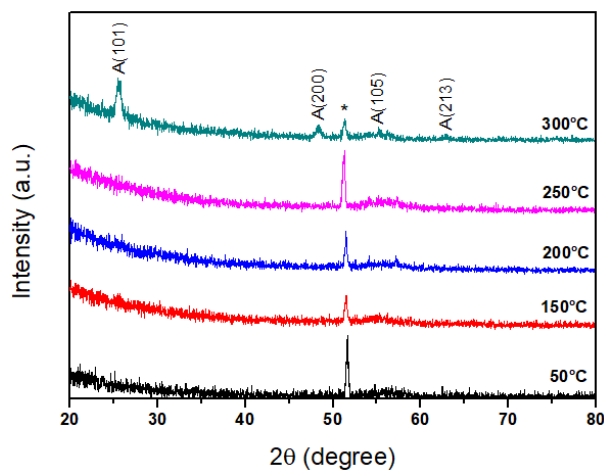
Figure 5.6 GIXRD spectra of TiO_2 thin films deposited at temperatures varying between 50 °C to 300 °C for 300 cycles. Curves have been shifted vertically for clarity. The asterisk shows substrate-related reflections.

AFM phase images of TiO$_2$ thin films grown at deposition temperatures of 250 °C and 300 °C for 300 cycles are shown in Figure 5.7(a) and Figure 5.7(b), respectively. The AFM image of 250 °C film does not show any distinct crystalline features which is consistent with the GIXRD data of this film (see Figure 5.6). On the other hand, as can be seen in Figure 5.7(b), clusters started to form in the film deposited at 300 °C during anatase phase formation. The diameters of the nanoclusters that are seen from the AFM phase image of this film are in the range of 10-20 nm.
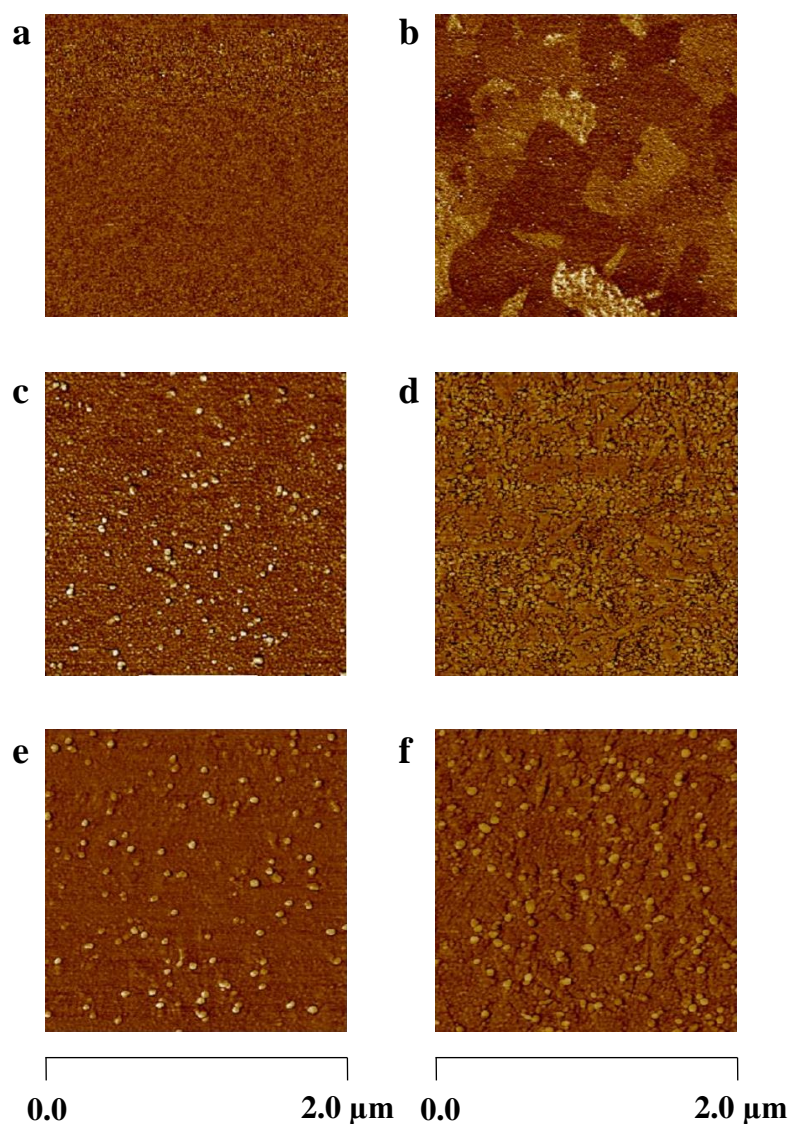
Figure 5.7 AFM phase images of TiO$_2$ thin films as-deposited for 300 cycles at substrate temperatures of (a) 250 °C and (b) 300 °C; for 700 cycles at (c) 250 °C and (d) 300 °C; and post-annealed at (e) 300 °C and (f) 350 °C for 1 hour after being deposited at 250 °C for 700 cycles.

GIXRD spectra of TiO$_2$ thin films grown at substrate temperatures of 250 °C and 300 °C for 700 cycles are presented in Figure 5.8. It is seen that no phase change was observed for the film deposited at 250 °C with increasing the number of cycles from 300 to 700. For the case of the film deposited at 300 °C, diffraction peaks of rutile phase were detected along with anatase, which reveals the transformation to rutile phase with increasing the number of cycles to 700. This can be attributed to the instantaneous non-uniform annealing during the long deposition duration of 700 cycles. This behavior was not detected for the film deposited at 250 °C for the same number of cycles, suggesting that 250 °C is not sufficient to induce local annealing to form any crystalline phases.
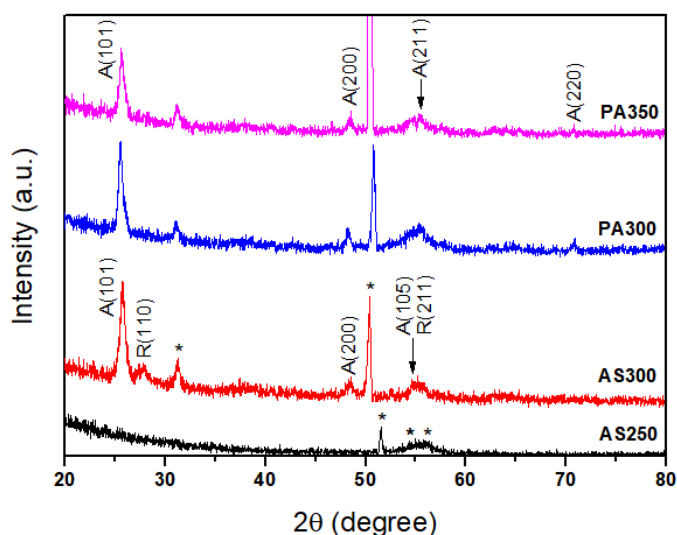
Figure 5.8 GIXRD spectra of TiO$_2$ thin films as-deposited for 700 cycles at temperatures 250 °C (AS250) and 300 °C (AS300), and post-annealed at 300 °C (PA300) and 350 °C (PA350) after being deposited at 250 °C for 700 cycles. Curves have been shifted vertically for clarity. The asterisk shows substrate-related reflections.

AFM phase images of the 700 cycle films are demonstrated in Figure 5.7(c) and Figure 5.7(d), respectively. Figure 5.7(c) shows the growth of nanosized grains on an amorphous background with a total surface roughness of 0.30 nm although the film was found to be amorphous from GIXRD measurement. Figure 5.7(d) reveals the formation of island-like structures of 200-300 nm in length in the 300 °C film with the increase in number of cycles to 700. The diameters of the spherical particles are mostly

around 80 nm. The relatively distinct surface morphology of this film may be originated from its anatase-rutile polycrystalline nature.

Figure 5.8 also shows the diffraction patterns of the two TiO_2 thin films deposited at 250 °C during 700 cycles and post-annealed at 300 °C and 350 °C for 1 hour, exhibiting the influence of post-deposition annealing on crystalline phase formation. Rutile formation was not observed for the post-annealed films unlike the as-deposited film grown at 300 °C for 700 cycles.

It can be seen from Figure 5.7(e) that the film deposited at 250 °C and post-annealed at 300 °C had a similar surface morphology to that of the as-deposited film at 250 °C. The post-annealed film exhibited larger particles with diameters in the range of 60-70 nm. On the other hand, Figure 5.7(f) demonstrates that the film deposited at 250 °C and post-annealed at 350 °C showed island-like nanostructures along with grain clusters resembling the as-deposited film at 300 °C. The spherical particles are measured to be 50-90 nm in diameter.

Although particle size can be measured from AFM images as mentioned above, since there may be defects inside the deposited films, crystallite size was also calculated. Calculated average crystallite sizes using GSAS/EXPGUI for different deposition conditions are given in Table 5.1 with chi square values. It is seen from Table 5.1, for the film deposited at 300 °C, the anatase crystallite size increases from 12 ± 1 nm to 30 ± 2 nm when the number of deposition cycles is increased from 300 to 700. The film deposited at 250 °C for 700 cycles and post-annealed at 350 °C exhibits larger crystallite size of 45 ± 2 nm when compared to the film deposited at 250 °C for 700 cycles and post-annealed at 300 °C, which exhibits crystallite size of 26 ± 2 nm. This suggests that the particle sizes that were directly measured from the AFM phase images might indicate either a single crystallite or multiple crystallites forming a particle with stacking faults or twinings.

Table 5.1 Calculated average crystallite sizes for TiO_2 thin films.

Substrate temperature (°C)	Number of cycles	Post-deposition annealing	Average crystallite size (nm)	Chi-square
300	300	-	12 ± 1	2.267 - 2.307
300	700	-	30 ± 2 (anatase) 15 ± 2 (rutile)	2.404 - 2.491
250	700	300 °C, 1h	26 ± 2	3.119 - 3.319
250	700	350 °C, 1h	45 ± 2	2.532 - 2.713

The rise in the surface roughness of the films deposited at 250 °C and 300 °C when the number of process cycles was increased from 300 to 700 cycles is presented in Figure 5.9. The roughness of the 300 cycle films deposited at 250 °C and 300 °C are 0.13 and 0.15 nm, respectively, while the roughness of the cSi substrate is 0.125. As the number of cycles was increased to 700, roughness of the films deposited at 250 °C and 300 °C became 0.30 and 1.02, respectively. It can be concluded from these results that for lower process cycles the films tend to mimic the roughness of the substrate. For the case of higher number of cycles, the monolayers become more susceptible to the changes in the film structure caused by the reaction chemistry.

Post-deposition annealing significantly influenced the surface roughness. The surface roughness of the two films as-deposited at 250 °C became 0.59 and 0.82 after post-annealing at 300 °C and 350 °C, respectively. Although surface roughness increases with post-annealing as compared to as-deposited samples, all films can be considered smooth.
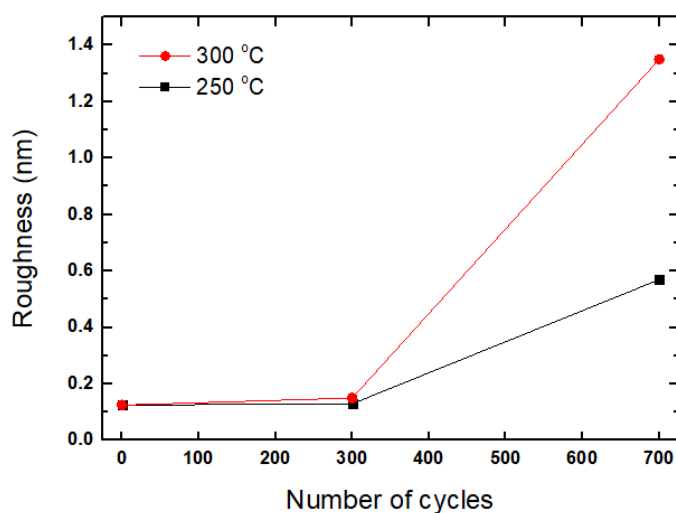
Figure 5.9 RMS surface roughness of TiO$_2$ thin films deposited at 250 °C and 300 °C as a function of number of deposition cycles. The zero number of cycles represents the surface roughness of cSi substrate.

5.1.1.4 Optical Properties

The variation of band gap energy with respect to the deposition temperature of TiO$_2$ thin films deposited for 300 cycles is presented in Figure 5.10. The films deposited at substrate temperatures varying from 50 to 250 °C are known to be amorphous as confirmed from GIXRD measurements. Band gaps of these films vary between 3.38 and 3.29 eV. Similar values have been reported by Aarik et al. [113] and Abendroth et al. [138] for amorphous TiO$_2$ thin films grown by ALD.

In the temperature range 50 to 200 °C, band gap values exhibit a decreasing trend with increasing substrate temperature. This may be associated with the beginning of crystallization in the nanoscale as the deposition temperature was increased. However, the band gap starts to increase beginning from the deposition temperature 230 °C and reaches a value of 3.33 eV for the 300 °C film, which is known to contain anatase phase. For anatase TiO$_2$ thin films, the reported band gap is in the range of 3.15 - 3.26 eV [53], [113], [155]. The relatively higher band gap of the 300 °C film in comparison to the literature data might be a result of the dominance of the amorphous fraction over the anatase.
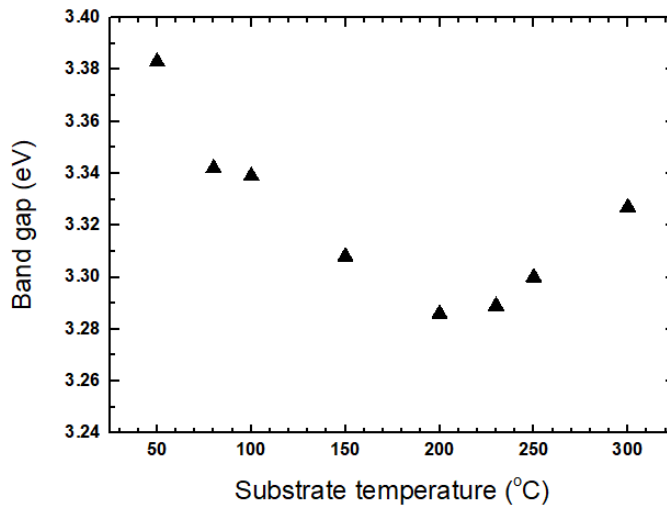
Figure 5.10 Band gap energy values of TiO$_2$ thin films as a function of number of substrate temperature.

Figure 5.11(a) and Figure 5.11(b) demonstrate the dependences of the refractive index and the extinction coefficient on deposition temperature as a function of wavelength. For all films, the extinction coefficient has a value of zero at wavelengths longer than 375 nm.

The change in the refractive index specifically at 632 nm as a function of deposition temperature is shown in Figure 5.12. Initially, the refractive index of the TiO$_2$ thin films increases from 2.15 to 2.22 with increasing temperature from 50 °C to 100 °C. The rather sharp increase at this low temperature region may be originated from the increasing film density, which may also be correlated with the increasing O/Ti ratio in the same temperature range. The amorphous TiO$_2$ thin films deposited at substrate temperatures from 100 °C to 250 °C exhibit a more stable region with refractive indices ranging between 2.22 and 2.23. Further increasing the growth temperature to 300 °C results in a refractive index of 2.26 due to the formation of anatase phase.
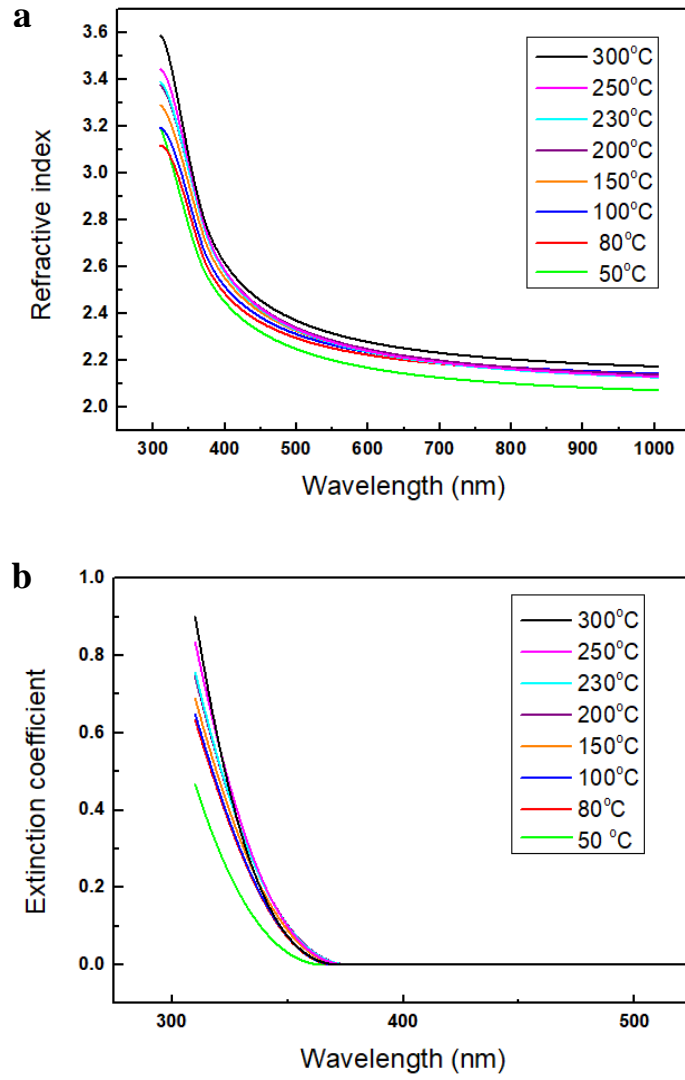
Figure 5.11 (a) Refractive index and (b) extinction coefficient curves of TiO$_2$ thin films deposited at different substrate temperatures as a function of wavelength.
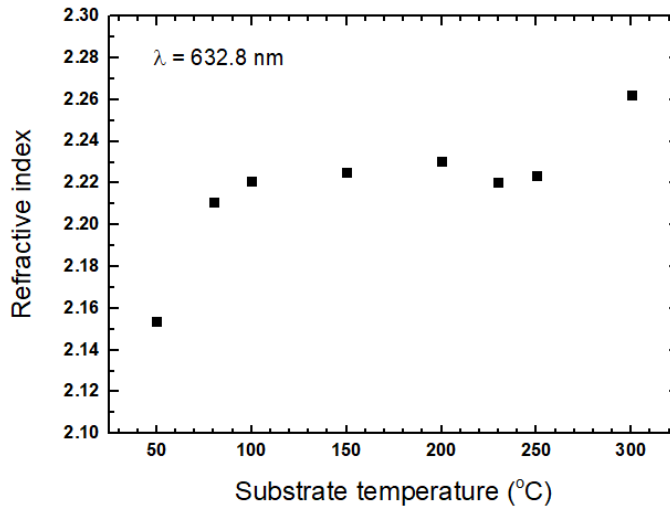
Figure 5.12 Variation of the refractive index at 632.8 nm as a function of substrate temperature.

5.2 Coaxial Nanowires

In order to investigate the effect of the refractive index on optical response, coaxial nanowires with Al_2O_3 spacer layer were also produced along with TiO_2 deposited coaxial nanowires. Al_2O_3 has a relatively low refractive index (i.e. 1.61-1.66 for amorphous Al_2O_3 produced with ALD) compared to that of TiO_2 (i.e. 2.2-2.4 for amorphous TiO_2 produced with ALD) [113], [156].

5.2.1 Morphological Characterization

- Core silver nanowires

SEM micrographs of Ag nanowires before and after annealing are shown in Figure 5.13(a) and Figure 5.13(b), respectively. The PVP layer around a single Ag nanowire is clearly seen in Figure 5.13(a). Figure 5.13(b) demonstrates that the PVP layer was removed after annealing at 200 °C for 1h.
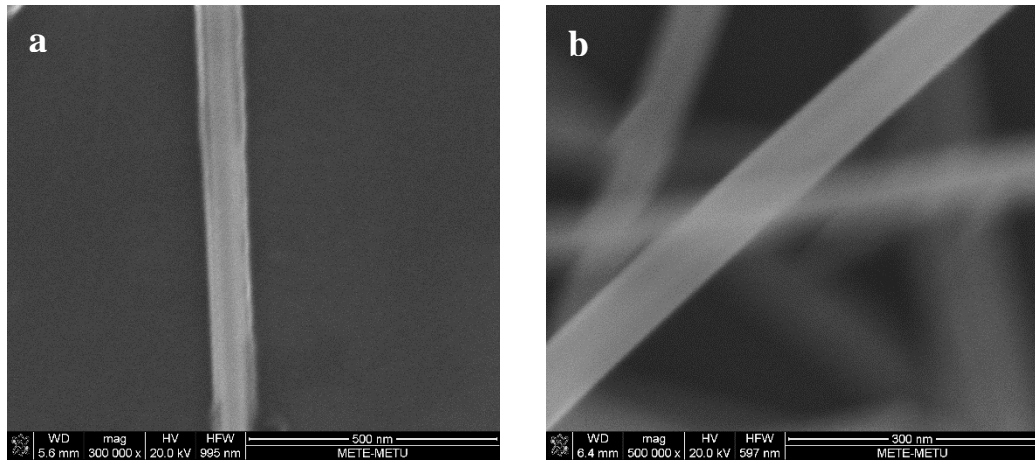
Figure 5.13 (a) Ag nanowires before annealing. The PVP layer is seen around the Ag nanowire. (b) Ag nanowires after annealing. The PVP layer is removed.

- TiO₂ and Al₂O₃ deposited silver nanowires

SEM micrographs of ALD TiO_2 around Ag nanowires deposited at 150 ℃ for 400 cycles are seen in Figure 5.14(a) and Figure 5.14(b). Figure 5.14(c) shows ALD Al_2O_3 around Ag nanowires deposited at 150 ℃ for 400 cycles. It is seen that the TiO_2 and Al_2O_3 coatings are quite conformal and uniform.
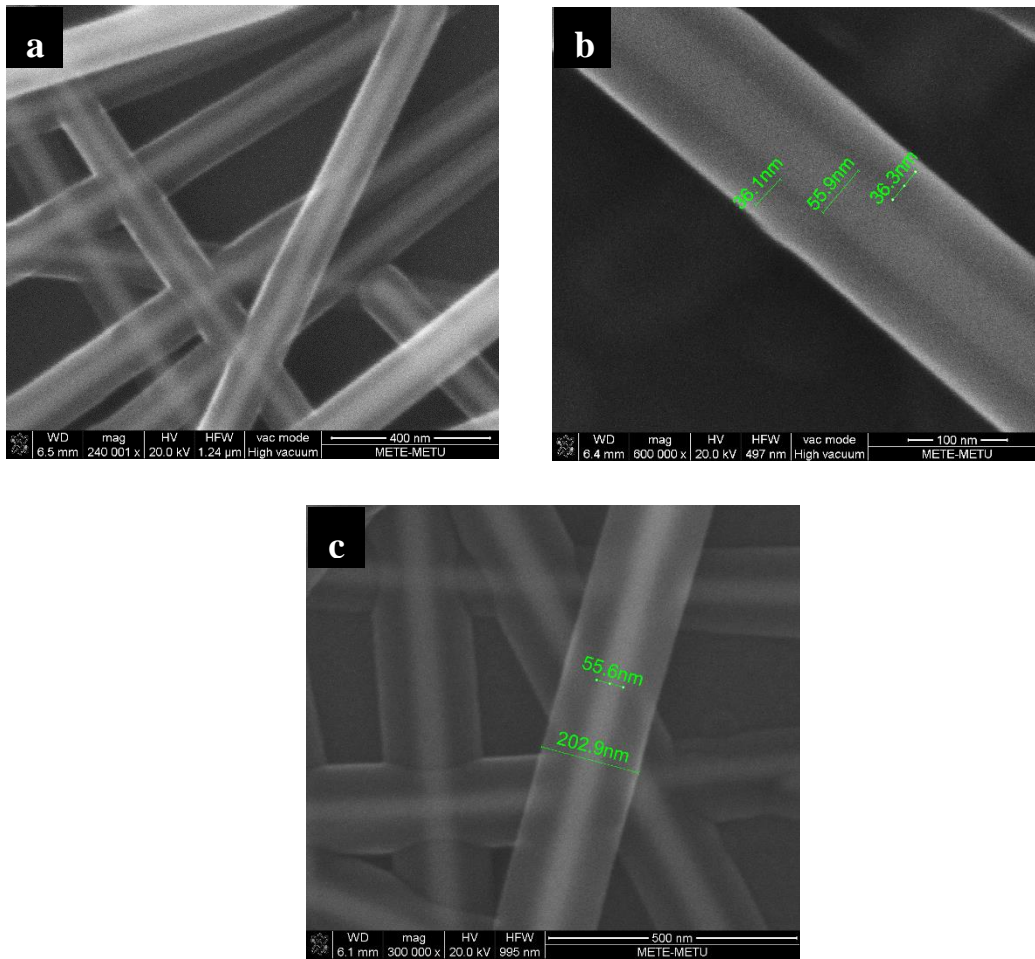
Figure 5.14 (a), (b) ALD TiO$_2$ around Ag nanowires deposited at 150 ℃ for 400 cycles, and (c) ALD Al$_2$O$_3$ around Ag nanowires deposited at 150 ℃ for 400 cycles.

5.2.2 Optical Characterization

5.2.2.1 Silver/Titania/Silver Coaxial Nanowires

Silver/titania/silver coaxial nanowires were produced for three different number of ALD process cycles: 200 cycles (thickness of ~ 10 nm), 200 cycles (thickness of ~ 15 nm), and 300 cycles (thickness of ~ 20 nm).

Transmittance, reflectance, and extinction curves for three different TiO$_2$ deposition thicknesses are shown in Figure 5.15, Figure 5.16, and Figure 5.17.

The transmittance spectra for all cases show that the bare Ag NWs exhibit a dip around 350 nm at the LSPR of silver. On the other hand, TiO$_2$ deposited Ag NWs exhibit a second dip around 450 nm due to the propagating surface plasmons in addition to the

dip around 350 nm caused by the localized surface plasmons. This suggests that the replacement of air-Ag interface with TiO_2-Ag interface enabled the formation of propagating surface plasmons.

The reflectance curves for all cases also demonstrate the existence of the LSPR around 350 nm.

The extinction curves for all cases reveal the existence of a second surface plasmon mode that is formed when the TiO_2/Ag NWs were coated with the top Ag layer, i.e. forming coaxial NWs. The smooth TiO_2 films deposited with ALD results in two symmetric Ag-TiO_2 interfaces in coaxial NWs. The formation of the second surface plasmon mode may be attributed to the hybridization of the two propagating surface plasmon modes formed at these symmetric Ag-TiO_2 interfaces.
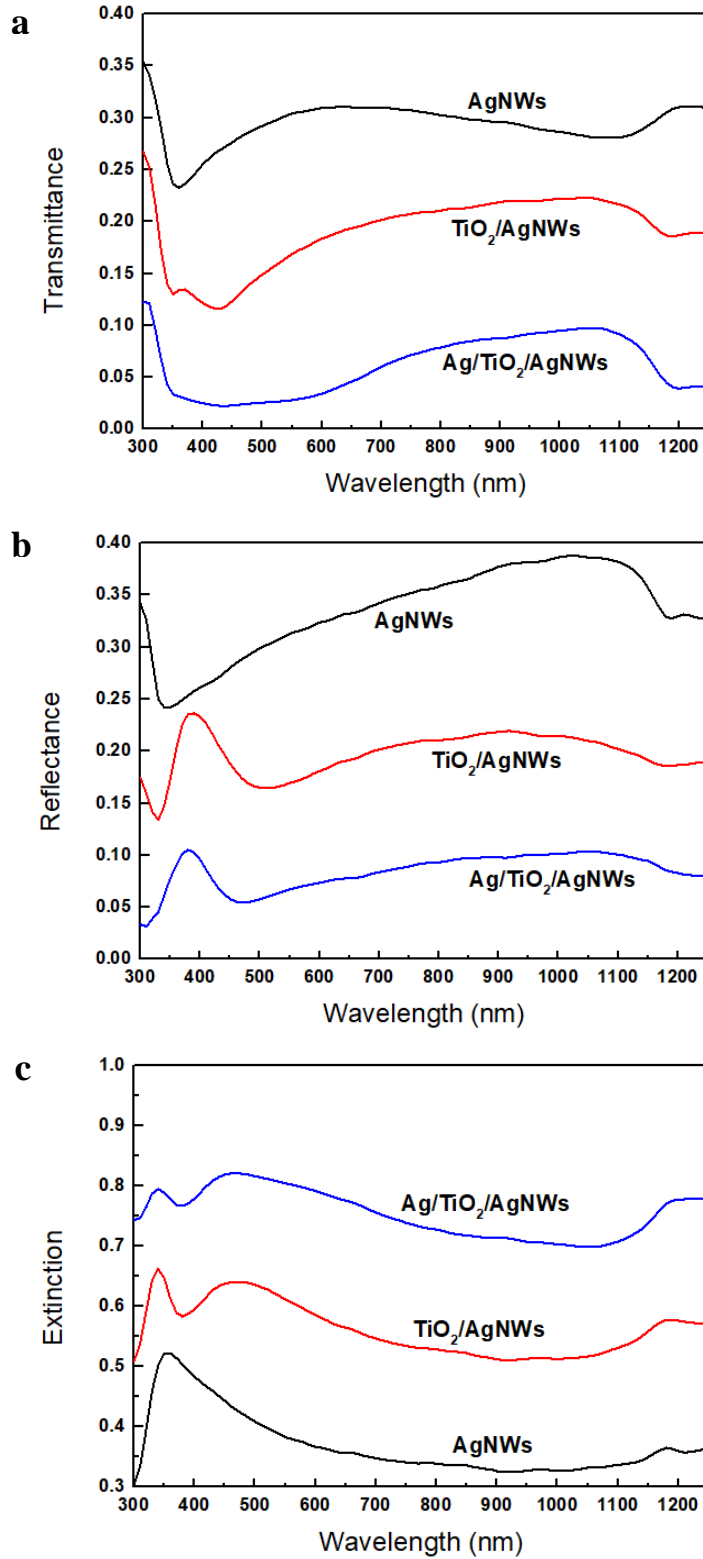
Figure 5.15 (a) Transmittance, (b) reflectance, and (c) extinction spectra for bare Ag NWs, 200 cycle TiO$_2$ deposited Ag NWs, and coaxial NWs. The curves were shifted vertically for clarity.
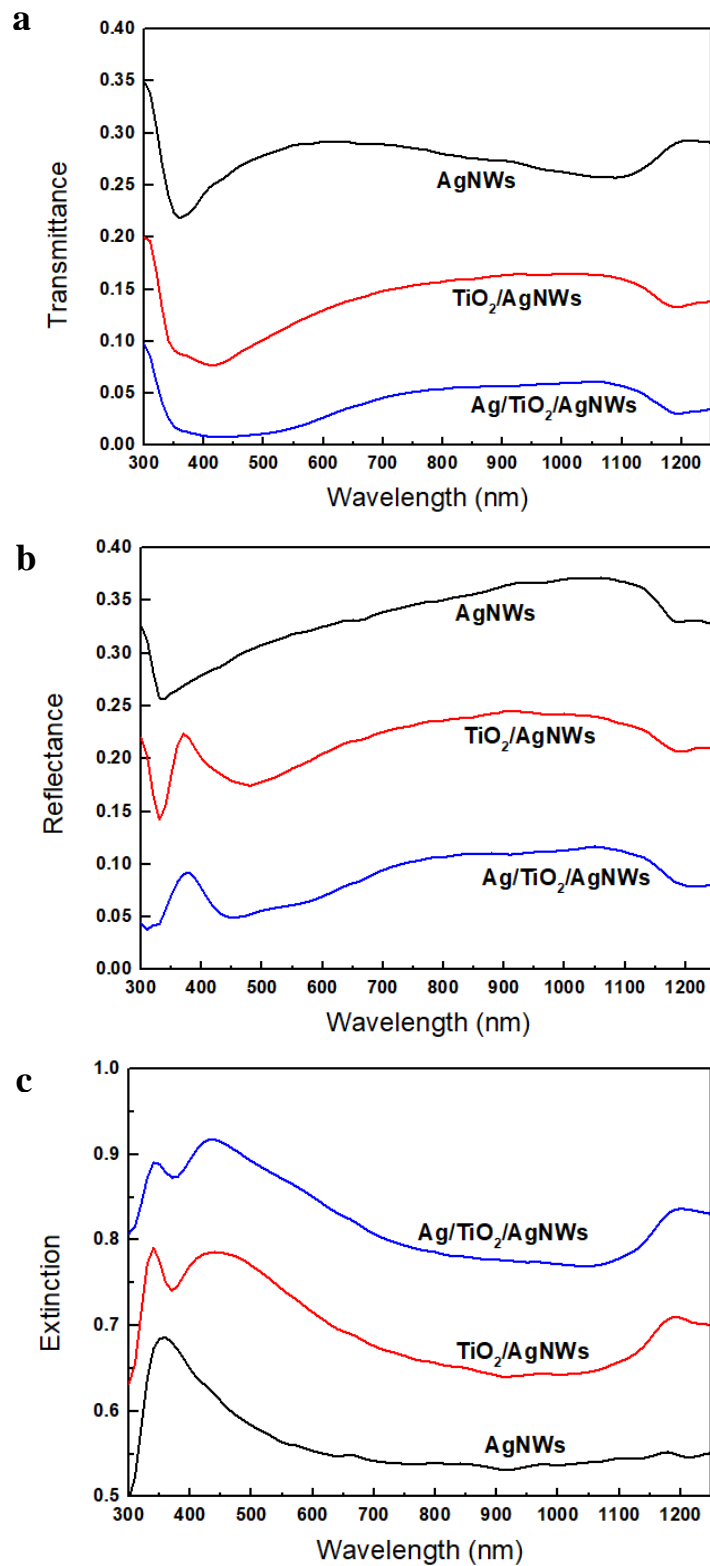
Figure 5.16 (a) Transmittance, (b) reflectance, and (c) extinction spectra for bare Ag NWs, 300 cycle TiO$_2$ deposited Ag NWs, and coaxial NWs. The curves were shifted vertically for clarity.
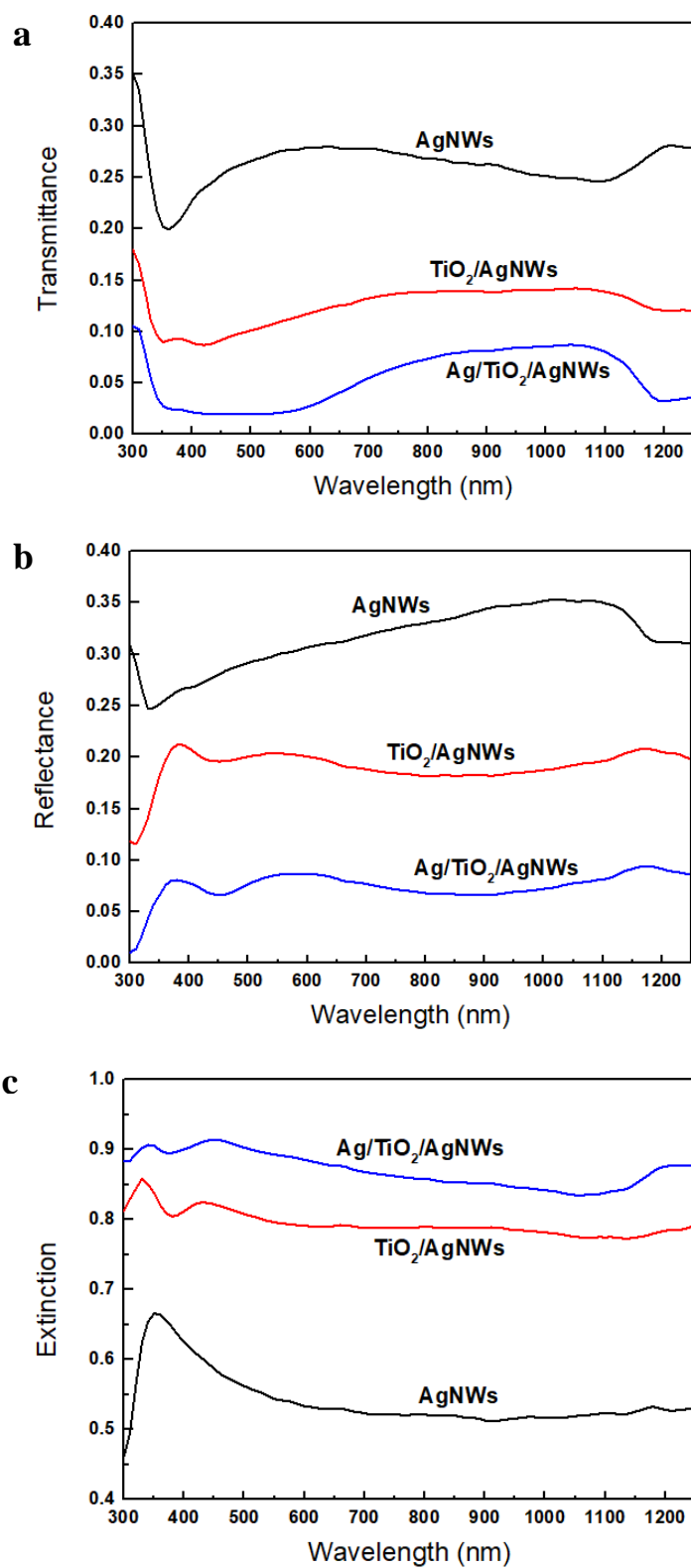
Figure 5.17 (a) Transmittance, (b) reflectance, and (c) extinction spectra for bare Ag NWs, 400 cycle TiO₂ deposited Ag NWs, and coaxial NWs. The curves were shifted vertically for clarity.
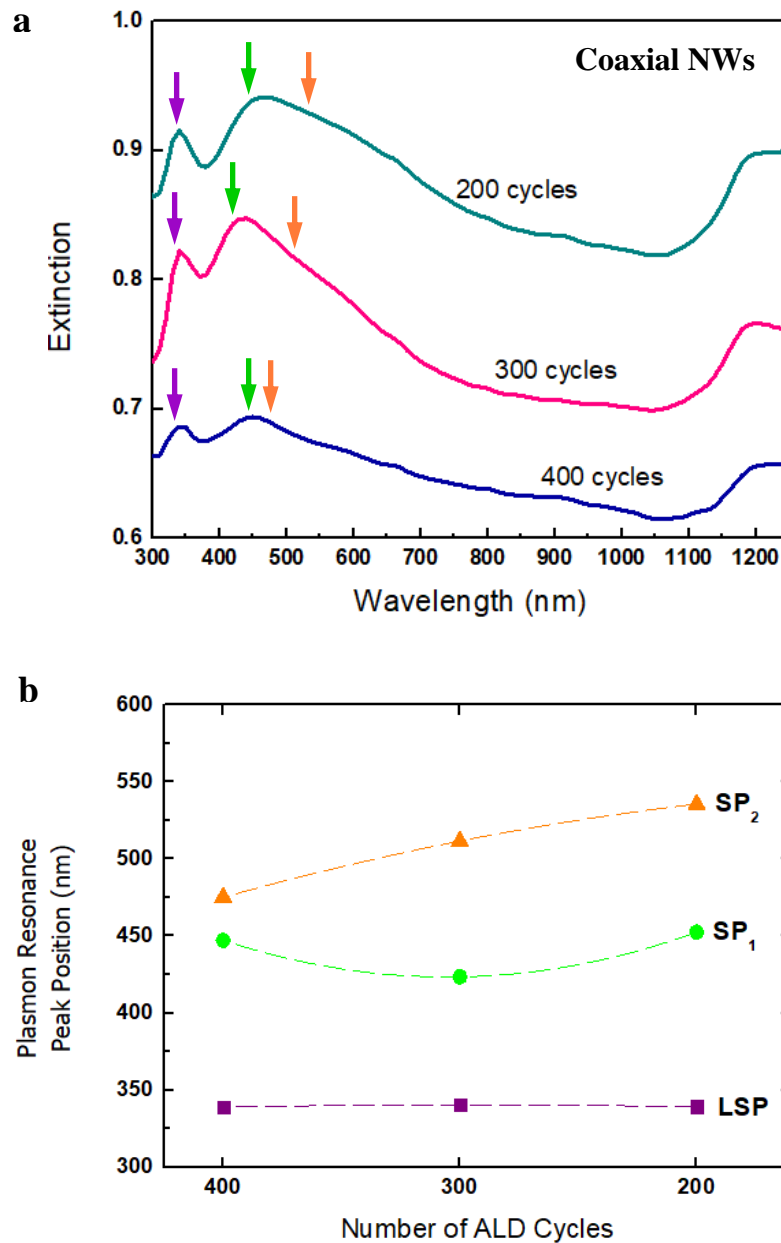
Figure 5.18 The comparison of (a) the extinction curves, and (b) the plasmon resonance peak positions for coaxial NWs with 200,300, and 400 cycle TiO_2 films. The extinction curves were shifted vertically for clarity.

The comparison of the extinction curves and the plasmon resonance peak positions for different ALD cycle coaxial nanowire samples are given in Figure 5.18(a) and Figure 5.18(b). The thinner TiO_2 films allow a better interaction between the surface plasmons formed at the Ag-TiO_2 interfaces, causing a stronger surface plasmon coupling. As a result, the energetic separation between the surface plasmons increases. This effect can be seen from Figure 5.18(b) showing the increased peak separation with decreased

TiO$_2$ thickness. These shifts in plasmon resonances and the emergence of a new surface plasmon mode for the case of coaxial NWs indicate the surface plasmon hybridization.

5.2.2.2 Silver/Alumina/Silver Coaxial Nanowires

Silver/alumina/silver coaxial nanowires were produced for three different number of ALD process cycles: 100 cycles (thickness of ~ 18 nm), 200 cycles (thickness of ~ 35 nm), and 300 cycles (thickness of ~ 53 nm).

Transmittance, reflectance, and extinction curves for three different Al$_2$O$_3$ deposition thicknesses are shown in Figure 5.19, Figure 5.20, and Figure 5.21.

The transmittance spectra for all cases show the LSP mode around 350 nm.

The extinction curves reveal the existence of a propagating surface plasmon mode along with the LSP mode when the Al$_2$O$_3$/Ag NWs were coated with the top Ag layer, i.e. forming coaxial NWs.
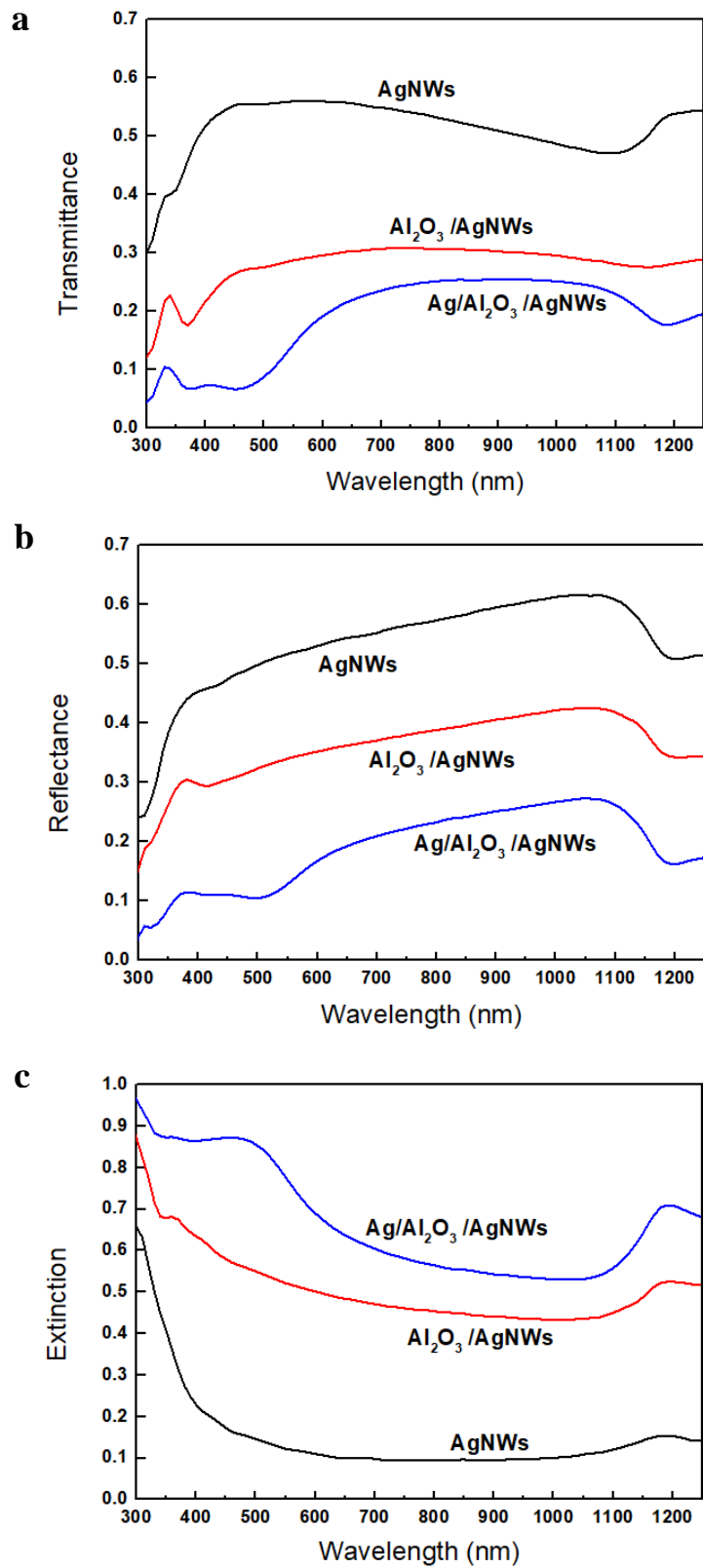
Figure 5.19 (a) Transmittance, (b) reflectance, and (c) extinction spectra for bare Ag NWs, 100 cycle Al_2O_3 deposited Ag NWs, and coaxial NWs. The curves were shifted vertically for clarity.
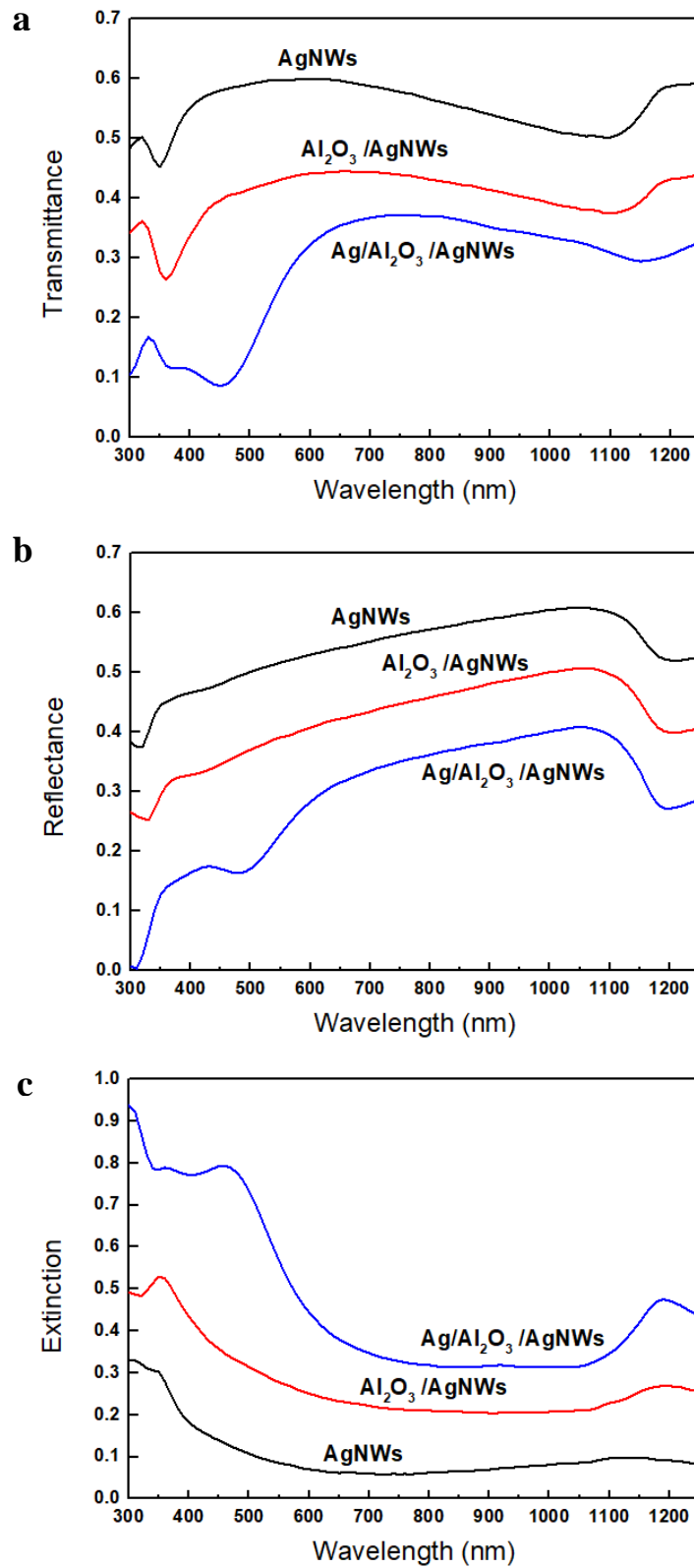
Figure 5.20 (a) Transmittance, (b) reflectance, and (c) extinction spectra for bare Ag NWs, 200 cycle Al_2O_3 deposited Ag NWs, and coaxial NWs. The curves were shifted vertically for clarity.
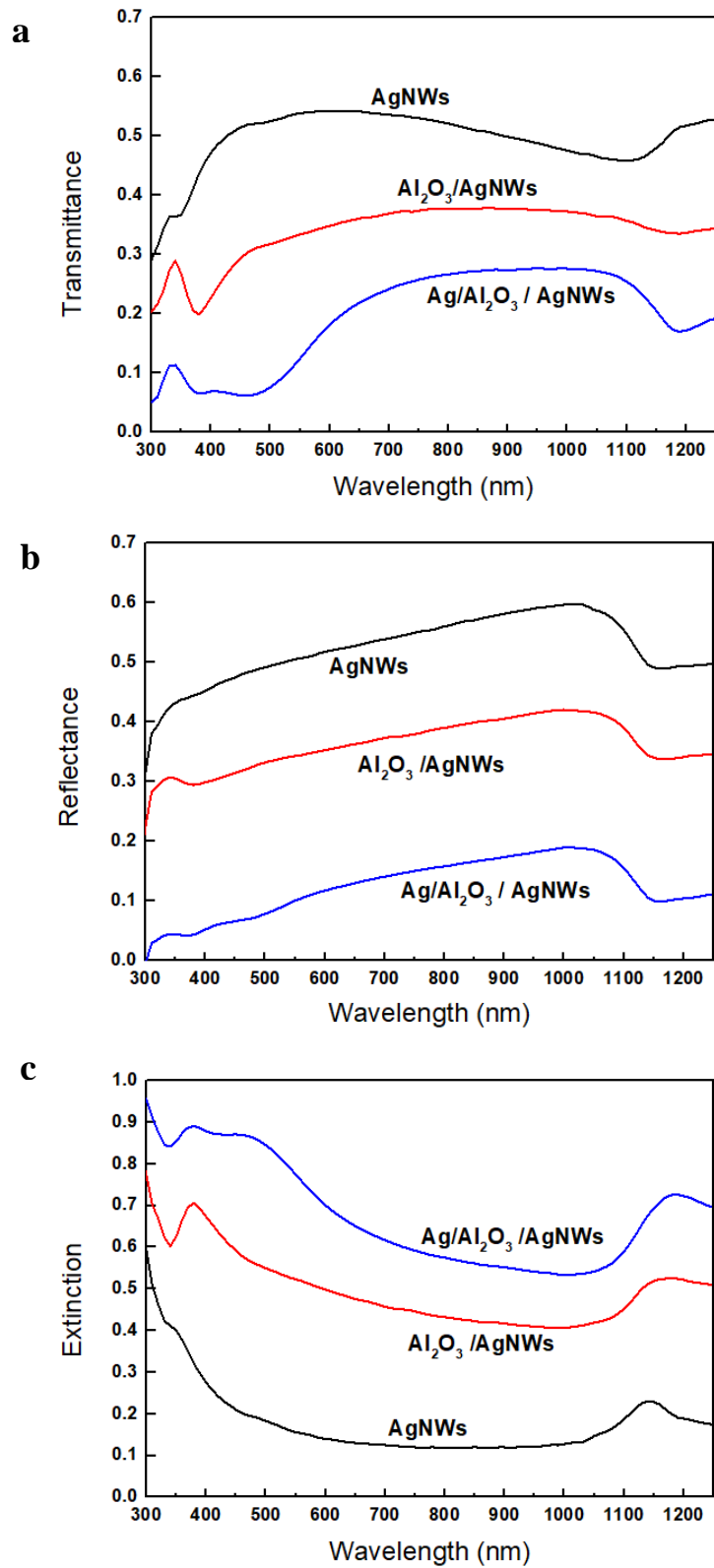
Figure 5.21 (a) Transmittance, (b) reflectance, and (c) extinction spectra for bare Ag NWs, 300 cycle Al_2O_3 deposited Ag NWs, and coaxial NWs. The curves were shifted vertically for clarity.

The comparison of the extinction curves and the plasmon resonance peak positions for different ALD cycle coaxial nanowire samples are given in Figure 5.22(a) and Figure 5.22(b). As in the case for TiO_2, in coaxial NWs with thinner Al_2O_3 films, the energetic separation between the surface plasmons increases. This effect can be seen from Figure 5.22(b) showing the increased peak separation with decreased Al_2O_3 thickness.
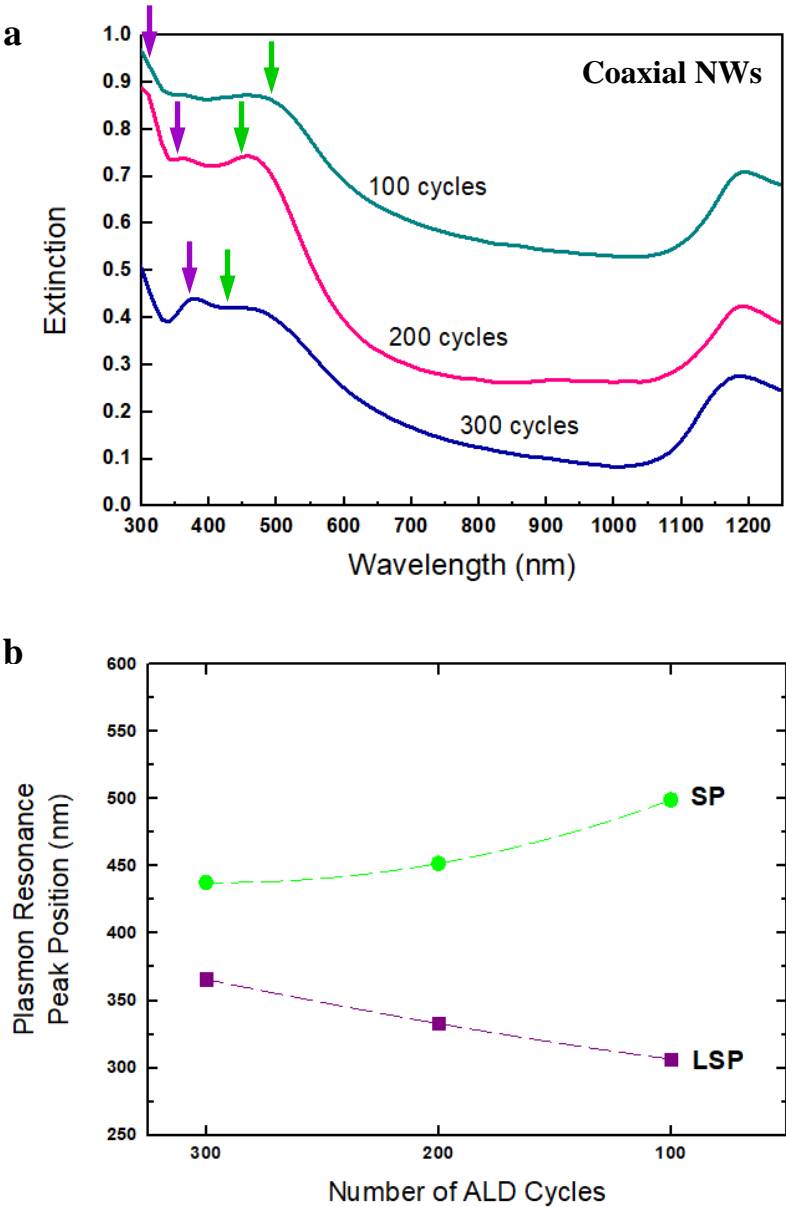
Figure 5.22 The comparison of (a) the extinction curves, and (b) the plasmon resonance peak positions for coaxial NWs with 100, 200, and 300 cycle Al_2O_3 films. The extinction curves were shifted vertically for clarity.

The penetration depth of the surface plasmons decreases as the refractive index of the dielectric medium increases. As a result, plasmon hybridization can occur in a shorter distance which is perpendicular to the surface. Since TiO_2 has a higher refractive index (i.e. ~ 2.2) compared to Al_2O_3 (i.e. ~ 1.6), the penetration depth of the surface plasmons is expected to decrease. Therefore, plasmon hybridization is expected in thinner TiO_2 films whereas Al_2O_3 also allows plasmon hybridization with increased film thickness. This phenomenon was observed in this study by preparing coaxial nanowires with thinner TiO_2 films and with thicker Al_2O_3 films.

CONCLUSIONS

In this thesis, it was aimed to enhance optical properties of low dimensional nanostructures via tailoring their plasmonic properties. Since low dimensional multilayered nanostructures support hybridized plasmon modes, 1D metal/dielectric/metal nanowires were produced and characterized. In order to obtain highly conformal and smooth dielectric layers, ALD technique was utilized.

First, ALD TiO_2 process was optimized by depositing TiO_2 thin films at substrate temperatures ranging between 50 ℃ and 300 ℃ for 300 cycles. A narrow ALD window with a stable growth rate of 0.65 Å/cycle was determined between 130 ℃ and 150 ℃. All films were found to be sub-stoichiometric. The films deposited at substrate temperatures below 300 ℃ were amorphous, whereas the film deposited at 300 ℃ contained anatase nanocrystals.

When the number of cycles was increased from 300 to 700, the film deposited at 300 ℃ were found to contain rutile nanocrystals along with anatase. The surface roughness values of the 250 ℃ and 300 ℃ films increased from 0.13 nm and 0.15 nm to 0.30 nm and 1.02 nm, respectively, as the number of cycles was increased from 300 to 700. Post-deposition annealing of the 250 ℃ film deposited for 700 cycles resulted in anatase phase formation.

Polyol synthesized 1D Ag nanowires were used as the core nanostructures. Since the scattering spectra of multilayered nanostructures depend strongly on the thicknesses of the layers, coaxial nanowire samples with three different TiO_2 thicknesses (i.e. 10 nm, 15 nm, and 20 nm) were prepared. 5 nm thick Ag layers were deposited on top of TiO_2 deposited Ag nanowires.

A second set of coaxial nanowires were produced with three different Al_2O_3 thicknesses (i.e. 18 nm, 35 nm, and 53 nm) to show the effect of the refractive index of the dielectric material on plasmonic response.

Both in TiO_2 and Al_2O_3 coaxial nanowires, localized and propagating surface plasmon modes were identified. As the thickness of the dielectric film decreased, the energetic separation between the surface plasmons increased.

Since TiO_2 is a higher refractive index material, plasmon hybridization in thinner films was observed whereas Al_2O_3 coaxial nanowires allowed plasmon hybridization in

thicker films. This suggests that TiO_2 allows confinement of the electric field in smaller volumes, which enables the use of TiO_2 coaxial nanowires with smaller dimensions. Finally, it was shown that the plasmonic response of 1D coaxial nanowires of metal-dielectric-metal multilayers can be tuned by tailoring the refractive index and the thickness of the constituent layers.

REFERENCES

[1]   S. Pillai and M. A. Green, "Plasmonics for photovoltaic applications," *Sol. Energy Mater. Sol. Cells*, vol. 94, no. 9, pp. 1481–1486, 2010.

[2]   P. Mandal and S. Sharma, "Progress in plasmonic solar cell efficiency improvement : A status review," *Renew. Sust. Energ. Rev.*, vol. 65, pp. 537–552, 2016.

[3]   X. Guo, Y. Ma, Y. Wang, and L. Tong, "Nanowire plasmonic waveguides, circuits and devices," *Laser Photonics Rev.*, vol. 7, no. 6, pp. 855–881, 2013.

[4]   P. Kumar, M. K. Wiedmann, C. H. Winter, and I. Avrutsky, "Optical properties of Al_2O_3 thin films grown by atomic layer deposition," *Appl. Opt.*, vol. 48, no. 28, pp. 5407–5412, 2009.

[5]   M. Faraday, "The Bakerian lecture: experimental relations of gold (and other metals) to light," *Phil. Trans. R. Soc. Lond.*, vol. 147, pp. 145–181, 1857.

[6]   D. Thompson, "Michael Faraday's recognition of ruby gold: the birth of modern nanotechnology," *Gold Bull.*, vol. 40, no. 4, pp. 267–269, 2007.

[7]   R. Zsigmondy and J. Alexander, *Colloids and the ultramicroscope; a manual of colloid chemistry and ultramicroscopy*. New York: John Wiley & Sons, 1909.

[8]   J. C. Maxwell, "A dynamical theory of the electromagnetic field," *Phil. Trans. R. Soc. Lond.*, vol. 155, pp. 459–512, 1865.

[9]   H. Horvath, "Gustav Mie and the scattering and absorption of light by particles: Historic developments and basics," *J. Quant. Spectrosc. Radiat. Transf.*, vol. 110, no. 11, pp. 787–799, 2009.

[10]   G. Mie, "Beitraege zur Optik trueber Medien speziell kolloidaler Goldloesungen (Contributions to the optics of diffuse media, especially colloid metal solutions)," *Ann. Phys.*, vol. 25, pp. 377–445, 1908.

[11]   D. Pines and D. Bohm, "Collective description of electron interactions: II. Collective vs individual particle aspects of the interactions," *Phys. Rev.*, vol. 85, no. 2, p. 338, 1952.

[12]   R. H. Ritchie, "Plasma losses by fast electrons in thin films," *Phys. Rev.*, vol. 106, no. 5, pp. 874–881, 1957.

[13]   M. Fleischmann, P. J. Hendra, and A. J. McQuillan, "Raman spectra of pyridine adsorbed at a silver electrode," *Chem. Phys. Lett.*, vol. 26, no. 2, pp. 163–166, 1974.

[14]   S. V. Gaponenko, *Introduction to Nanophotonics*. Cambridge University Press, 2010.

[15]   T. W. Ebbesen, H. J. Lezec, H. F. Ghaemi, T. Thio, and P. A. Wolff, "Extraordinary optical transmission through sub-wavelength hole arrays," *Nature*, vol. 391, no. February, pp. 667–669, 1998.

[16]   R. v. Baltz, "Plasmons and surface plasmons in bulk metals, metallic clusters, and metallic heterostructures," [Online]. Available: http://www-tkm.physik.uni-karlsruhe.de/personal/baltz/Er1995-Plasmons.pdf [Accessed: 15-Jan-2017].

[17]   S. A. Maier, *Plasmonics : Fundamentals and Applications*, Springer, 2004.

[18]   V. Palenskis, "Drift mobility , diffusion coefficient of randomly moving charge carriers in metals and other materials with degenerated electron gas," *WJCMP*, vol. 2013, no. February, pp. 73–81, 2013.

[19]   Y. Xia and N. J. Halas, "Shape-controlled synthesis and surface plasmonic properties of metallic nanostructures," *MRS Bull.*, vol. 30, no. 5, pp. 338–348, 2011.

[20]   M. Li, S. K. Cushing, and N. Wu, "Plasmon-enhanced optical sensors: a review," *Analyst*, vol. 140, no. 2, pp. 386–406, 2015.

[21]   J. M. Luther, P. K. Jain, T. Ewers, and A. P. Alivisatos, "Localized surface plasmon resonances arising from free carriers in doped quantum dots," *Nat. Mater.*, vol. 10, no. 5, pp. 361–366, 2011.

[22]   J. Homola, "Surface plasmon resonance sensors for detection of chemical and biological species," *Chem. Rev.*, vol. 108, no. 2, pp. 462–493, 2008.

[23]   M. Varga and J. Proke, "Electrical conductivity of polyaniline – silver nanocomposites," in *WDS'12*, 2012, no. Part III, pp. 52–57.

[24] R. J. Chimentão *et al.*, "Different morphologies of silver nanoparticles as catalysts for the selective oxidation of styrene in the gas phase.," *Chem. Commun. (Camb).*, no. 7, pp. 846–847, 2004.

[25] L. Zhang, B. Wang, G. Zhu, and X. Zhou, "Synthesis of silver nanowires as a SERS substrate for the detection of pesticide thiram," *Spectrochim. Acta - Part A Mol. Biomol. Spectrosc.*, vol. 133, pp. 411–416, 2014.

[26] X. Hu and C. T. Chan, "Photonic crystals with silver nanowires as a near-infrared superlens," *Appl. Phys. Lett.*, vol. 85, no. 9, pp. 1520–1522, 2004.

[27] P. Alivisatos, "The use of nanocrystals in biological detection.," *Nat. Biotechnol.*, vol. 22, no. 1, pp. 47–52, 2004.

[28] Q. Li, S. Wang, Y. Chen, M. Yan, L. Tong, and M. Qiu, "Experimental demonstration of plasmon propagation, coupling, and splitting in silver nanowire at 1550-nm wavelength," *IEEE J. Sel. Top. Quantum Electron.*, vol. 17, no. 4, pp. 1107–1111, 2011.

[29] B. Wild *et al.*, "Propagation lengths and group velocities of plasmons in chemically synthesized gold and silver nanowires," *ACS Nano*, vol. 6, no. 1, pp. 472–482, 2012.

[30] Q. Li and M. Qiu, "Plasmonic wave propagation in silver nanowires: guiding modes or not?," *Opt. Express*, vol. 21, no. 7, pp. 8587–8595, 2013.

[31] X. Guo, C. W. Guo, C. Wang, C. Li, and X. M. Sun, "AlGaInP LED with low-speed spin-coating silver nanowires as transparent conductive layer.," *Nanoscale Res. Lett.*, vol. 9, no. 1, p. 2495, 2014.

[32] J. Van de Groep, P. Spinelli, and A. Polman, "Transparent conducting silver nanowire networks," *Nano Lett.*, vol. 12, no. 6, pp. 3138–3144, 2012.

[33] H. Dong, Y. Chen, and C. Feldmann, "Polyol synthesis of nanoparticles: status and options regarding metals, oxides, chalcogenides, and non-metal elements," *Green Chem.*, vol. 17, pp. 4107–4132, 2015.

[34] S. Coskun, B. Aksoy, and H. E. Unalan, "Polyol synthesis of silver nanowires: An extensive parametric study," *Cryst. Growth Des.*, vol. 11, no. 11, pp. 4963–4969, 2011.

[35] Q. N. Luu, J. M. Doorn, M. T. Berry, C. Jiang, C. Lin, and P. S. May, "Preparation and optical properties of silver nanowires and silver-nanowire thin films," *J. Colloid Interface Sci.*, vol. 356, no. 1, pp. 151–158, 2011.

[36] H. Xu, H. Li, Z. Liu, S. Xie, X. Zhou, and J. Wu, "Adjustable plasmon resonance in the coaxial gold nanotubes," *Solid State Commun.*, vol. 151, no. 10, pp. 759–762, 2011.

[37] H. Tang, K. Prasad, R. Sanjines, P. E. Schmid, and F. Levy, "Electrical and optical properties of TiO_2 anatase thin films," *J. Appl. Phys.*, vol. 75, no. 4, pp. 2042–2047, 1994.

[38] S. H. Elder *et al.*, "The discovery and study of nanocrystalline TiO_2 - (MoO_3) core - shell materials," no. 38, pp. 5138–5146, 2000.

[39] S. Y. Kim, "Simultaneous determination of refractive index , extinction coefficient , and void distribution of titanium dioxide thin film by optical methods," *Appl. Opt.*, vol. 35, no. 34, pp. 6703–6707, 1996.

[40] H. Fukuda, S. Namioka, M. Miura, Y. Ishikawa, M. Yoshino, and S. Nomura, "Structural and electrical properties of crystalline TiO_2 thin films formed by metalorganic decomposition," *Jpn. J. Appl. Phys.,* vol. 38, pp. 6034–6038, 1999.

[41] G. Pfaff and P. Reynders, "Angle-dependent optical effects deriving from submicron structures of films and pigments," *Chem. Rev.*, vol. 99, no. 7, pp. 1963–1981, 1999.

[42] A. Salvador, M. C. Pascual-Martí, J. R. Adell, A. Requeni, and J. G. March, "Analytical methodologies for atomic spectrometric determination of metallic oxides in UV sunscreen creams," *J. Pharm. Biomed. Anal.*, vol. 22, no. 2, pp. 301–306, 2000.

[43] J. H. Braun, A. Baidins, and R. E. Marganski, "TiO_2 pigment technology: a review," *Prog. Org. Coatings*, vol. 20, no. 2, pp. 105–138, 1992.

[44] A. Weir, P. Westerhoff, L. Fabricius, and N. von Goetz, "Titanium dioxide nanoparticles in food and personal care products," *Environ. Sci. Technol.*, vol. 46, no. 4, pp. 2242–2250, 2012.

[45] A. Fujishima and K. Honda, "Electrochemical photolysis of water at a semiconductor electrode.," *Nature*, vol. 238, no. 5358, pp. 37–38, 1972.

[46] A. Mills and S. Le Hunte, "An overview of semiconductor photocatalysis," *J. Photochem. Photobiol. A Chem.*, vol. 108, no. 1, pp. 1–35, 1997.

[47]   A. L. Linsebigler, J. T. Yates Jr, and G. Lu, "Photocatalysis on TiO$_2$ Surfaces: Principles, mechanisms, and selected results," *Chem. Rev.*, vol. 95, no. 3, pp. 735–758, 1995.

[48]   M. Grätzel, "Photoelectrochemical cells," *Nature*, vol. 414, pp. 338–344, 2001.

[49]   V. Pore, "Atomic layer deposition and photocatalytic properties of titanium dioxide thin films," Ph.D. Dissertation, 2010.

[50]   B. Prasai, B. Cai, M. K. Underwood *et al.*, "Properties of amorphous and crystalline titanium dioxide from first principles," *J. Mater. Sci.*, vol.47, pp. 7515-7521, 2012.

[51]   Ç. Kılıç and A. Zunger, "n-type doping of oxides by hydrogen," *Appl. Phys. Lett.*, vol. 73, pp. 10–13, 2002.

[52]   Q. Cheng, W. Ahmad, G. Liu, and K. Wang, "Structural evolution of amorphous thin films of titanium dioxide," *11th IEEE International Conference on Nanotechnology*, pp. 1598-1601, 2011.

[53]   U. Diebold, "The surface science of titanium dioxide," *Surf. Sci. Rep.*, vol. 48, no. 5, pp. 53–229, 2003.

[54]   O. Sneh, R. B. Clark-phelps, A. R. Londergan, J. Winkler, and T. E. Seidel, "Thin film atomic layer deposition equipment for semiconductor processing," *Thin Solid Films*, *vol.* 402, pp. 248–261, 2002.

[55]   T. Suntola and J. Antson, "Method for producing compound thin films," US Patent 4,058,430, 1977.

[56]   T. Kääriäinen, D. Cameron, M.-L. Kääriäinen, and A. Sherman, *Atomic Layer Deposition: Principles, Characteristics, and Nanotechnology Applications*, 2nd ed., Scrivener, 2013.

[57]   M. Ritala and M. Leskelä, "Atomic layer deposition," in *Handbook of Thin Film Materials Volume 1: Deposition and Processing of Thin Films*, pp. 103–159, 2002.

[58]   J. R. Creighton and P. Ho, "Chapter 1: Introduction to chemical vapor deposition (CVD)," *Chem. Vap. Depos.*, pp. 1–13, 2001.

[59]   M. Leskelä and M. Ritala, "Atomic layer deposition (ALD): From precursors to thin film structures," *Thin Solid Films*, vol. 409, no. 1, pp. 138–146, 2002.

[60] S. M. George, "Atomic layer deposition: An overview," *Chem. Rev.*, vol. 110, p. 111, 2010.

[61] R. L. Puurunen, "Surface chemistry of atomic layer deposition: a case study for the trimethylaluminum/water process," *J. Appl. Phys.*, vol. 97, no. 12, pp. 121301-121301–52, 2005.

[62] S. Lindfors, A. Pakkala, and T. Suntola, "Apparatus for performing growth of compound thin films," US Patent No. 4,389,973, 1983.

[63] T. Suntola and J. Hyviirinen, "Atomic layer epitaxy," *Annu. Rev. Mater. Sci.*, vol. 15, pp. 177–195, 1985.

[64] A. A. Malygin, V. E. Drozd, A. A. Malkov, and V. M. Smirnov, "From V. B. Aleskovskii's 'framework' hypothesis to the method of molecular layering/atomic layer deposition," *Chem. Vap. Depos.*, vol. 21, no. 10–12, pp. 216–240, 2015.

[65] G. N. Parsons, S. M. George, and M. Knez, "Progress and future directions for atomic layer deposition and ALD-based chemistry," *MRS Bull.*, vol. 36, no. November, pp. 865–871, 2011.

[66] [Online]. Available: http://www.lumineq.com. [Accessed: 03-Dec-2016].

[67] P. Dosing *et al.*, "Atomic layer deposition of nanomaterials for Li-ion batteries, fuel cells, and solar cells and nanoparticles," pp. 117–120.

[68] J. W. Elam, N. P. Dasgupta, and F. B. Prinz, "ALD for clean energy conversion, utilization, and storage," *MRS Bull.*, vol. 36, no. November, pp. 899–906, 2011.

[69] J. W. E. X. Meng, "Atomic layer deposition of nanophase materials for electrical energy storage," in *ECS Trans.*, vol. 69, no. 7, pp. 39–57, 2015.

[70] A. Douglas, N. Muralidharan, R. Carter, K. Share, and C. L. Pint, "Ultrafast triggered transient energy storage by atomic layer deposition into porous silicon for integrated transient electronics," *Nanoscale*, vol.8, pp. 7384–7390, 2016.

[71] H. Puurunen, Riikka L, Saarilahti, J., Kattelus, "Implementing ALD layers in MEMS processing," in *ECS Trans.*, vol. 11, no. 7, pp. 3–14, 2007.

[72]   N. D. Hoivik, J. W. Elam, R. J. Linderman, V. M. Bright, S. M. George, and Y. C. Lee, "Atomic layer deposited protective coatings for micro-electromechanical systems," *Sensors Actuators A*, vol. 103, pp. 100–108, 2003.

[73]   M. K. Tripp, C. Stampfer, C. F. Herrmann, C. Hierold, S. George, and V. M. Bright, "Low stress atomic layer deposited alumina for nano electro mechanical systems," in *Transducers'05*, 2005, pp. 851–854.

[74]   B. D. Davidson, D. Seghete, S. M. George, and V. M. Bright, "Physical ALD tungsten NEMS switches and tunneling devices," *Sensors Actuators A. Phys.*, vol. 166, no. 2, pp. 269–276, 2011.

[75]   J. Camacho-bunquin *et al.*, "Catalyst synthesis and evaluation using an integrated atomic layer deposition synthesis – catalysis testing tool," *Rev. Sci. Instrum.*, vol. 86, no. 84103, 2015.

[76]   B. J. O. Neill *et al.*, "Catalyst design with atomic layer deposition," *ACS Catal.*, vol. 5, pp. 1804–1825, 2015.

[77]   M. Kemell, M. Ritala, M. Leskela, R. Groenen, and S. Lindsfor, "Coating of highly porous fiber matrices by atomic layer deposition" *Chem. Vap. Depos.*, vol. 14, no. 11–12, pp. 347–352, 2008.

[78]   A. K. Roy *et al.*, "Atomic layer deposition (ALD) as a coating tool for reinforcing fibers," *Anal. Bioanal. Chem.*, vol. 396, no. 5, pp. 1913–1919, 2010.

[79]   Key words used: atomic layer deposition, atomic layer chemical vapo(u)r deposition, atomic layer epitaxy, molecular lamination, molecular layer epitaxy, molecular layering.

[80]   V. Miikkulainen, M. Leskelä, M. Ritala, and R. L. Puurunen, "Crystallinity of inorganic films grown by atomic layer deposition: Overview and general trends," *J. Appl. Phys.*, vol. 113, no. 2, 2013.

[81]   R. L. Puurunen and W. Vandervorst, "Island growth as a growth mode in atomic layer deposition: A phenomenological model," *J. Appl. Phys.*, vol. 96, no. 12, pp. 7686–7695, 2004.

[82]   M. Ylilammi, "Monolayer thickness in atomic layer deposition," *Thin Solid Films*, vol. 279, pp. 124–130, 1996.

[83] H. Kim, "Atomic layer deposition of metal and nitride thin films: Current research efforts and applications for semiconductor device processing," *J. Vac. Sci. Technol. B Microelectron. Nanom. Struct.*, vol. 21, no. 6, pp. 2231–2261, 2003.

[84] H. Kim, "Characteristics and applications of plasma enhanced-atomic layer deposition," *Thin Solid Films*, vol. 519, no. 20, pp. 6639–6644, 2011.

[85] H. B. Profijt, S. E. Potts, M. C. M. van de Sanden, and W. M. M. Kessels, "Plasma-assisted atomic layer deposition: basics, opportunities, and challenges," *J. Vac. Sci. Technol. A Vacuum, Surfaces, Film.*, vol. 29, no. 5, p. 50801, 2011.

[86] "ALD advantages." [Online]. Available: http://www.cambridgenanotechald.com/atomic-layer-deposition/ald-advantages.shtml. [Accessed: 13-Dec-2016].

[87] "Aluminium oxide atomic layer deposition (ALD)." [Online]. Available: https://www.oxford-instruments.com/products/etching-deposition-and-growth/processes/deposition-processes/metal-oxides/al2o3-deposition/al2o3-plasma-and-thermal-ald-using-opal. [Accessed: 13-Dec-2016].

[88] A. Pourret, P. Guyot-Sionnest, and J. W. Elam, "Atomic layer deposition of ZnO in quantum dot thin films," *Adv. Mater.*, vol. 21, no. 2, pp. 232–235, 2009.

[89] N. P. N. Dasgupta, W. Lee, T. P. Holme, and F. B. Prinz, "Atomic layer deposition of PbS-ZnS quantum wells for high-efficiency solar cells," *(PVSC), 34th IEEE*, pp. 356–360, 2009.

[90] J. W. Elam, Z. A. Sechrist, and S. M. George, "ZnO/Al$_2$O$_3$ nanolaminates fabricated by atomic layer deposition: growth and surface roughness measurements," *Thin Solid Films*, vol. 414, no. 1, pp. 43–55, 2002.

[91] A. Szeghalmi, S. Senz, M. Bretschneider, U. Gösele, and M. Knez, "All dielectric hard x-ray mirror by atomic layer deposition," *Appl. Phys. Lett.*, vol. 94, no. 13, pp. 1–4, 2009.

[92] Stefan Riedel *et al.*, "Synthesis of SrTiO$_3$ by crystallization of SrO/TiO$_2$ superlattices prepared by atomic layer deposition," *J. Appl. Phys.*, vol. 109, no. 9, pp. 094101–094108, 2011.

[93]   P. Banerjee, W.-J. Lee, K.-R. Bae, S. B. Lee, and G. W. Rubloff, "Structural, electrical, and optical properties of atomic layer deposition Al-doped ZnO films," *J. Appl. Phys.*, vol. 108, no. 4, pp. 043504–043510, 2010.

[94]   S. J. Lim, S. J. Kwon, H. Kim, and J. S. Park, "High performance thin film transistor with low temperature atomic layer deposition nitrogen-doped ZnO," *Appl. Phys. Lett.*, vol. 91, no. 18, pp. 2013–2016, 2007.

[95]   J. R. Bakke and S. F. Bent, "Formation of $Cd_xZn_{1-x}S$ films for photovoltaic buffer layers by atomic layer deposition," in *ECS Trans.*, 2009, vol. 25, no. 4, pp. 9–14.

[96]   J. W. Elam and S. W. George, "Growth of ZnO/Al_2O_3 alloy films using atomic layer deposition techniques," *Chem. Mater.*, vol. 15, no. 4, pp. 1020–1028, 2003.

[97]   E. Dashjav, M. Lipińska-Chwałek, D. Grüner, G. Mauer, M. Luysberg, and F. Tietz, "Atomic layer deposition and high-resolution electron microscopy characterization of nickel nanoparticles for catalyst applications," *Surf. Coatings Technol.*, vol. 307, pp. 428–435, 2016.

[98]   S. Seong, Y. C. Jung, T. Lee, I.-S. Park, and J. Ahn, "Fabrication of Fe_3O_4-ZnO core-shell nanoparticles by rotational atomic layer deposition and their multi-functional properties," *Curr. Appl. Phys.*, vol. 16, no. 12, pp. 1564–1570, 2016.

[99]   M. G. Jeong, I. H. Kim, S. W. Han, D. H. Kim, and Y. D. Kim, "Room temperature CO oxidation catalyzed by NiO particles on mesoporous SiO_2 prepared via atomic layer deposition: Influence of pre-annealing temperature on catalytic activity," *J. Mol. Catal. A Chem.*, vol. 414, pp. 87–93, 2016.

[100]   F. Muñoz-Muñoz *et al.*, "The control of thickness on aluminum oxide nanotubes by atomic layer deposition using carbon nanotubes as removable templates," *Powder Technol.*, vol. 286, pp. 602–609, 2015.

[101]   I. Donmez, F. Kayaci, C. Ozgit-Akgun, T. Uyar, and N. Biyikli, "Fabrication of hafnia hollow nanofibers by atomic layer deposition using electrospun nanofiber templates," *J. Alloys Compd.*, vol. 559, pp. 146–151, 2013.

[102]   W. Zhang, T. Qiu, X. P. Qu, and P. K. Chu, "Atomic layer deposition of platinum thin films on anodic aluminium oxide templates as surface-enhanced Raman scattering substrates," *Vacuum*, vol. 89, no. 1, pp. 257–260, 2013.

[103] H. C. Guo, E. Ye, Z. Li, M.-Y. Han, and X. J. Loh, "Recent progress of atomic layer deposition on polymeric materials," *Mater. Sci. Eng. C*, vol. 70, pp. 1–10, 2016.

[104] H. Ceylan *et al.*, "Size-controlled conformal nanofabrication of biotemplated three-dimensional TiO_2 and ZnO nanonetworks.," *Sci. Rep.*, vol. 3, p. 2306, 2013.

[105] M. Knez, A. Kadri, C. Wege, U. Gösele, H. Jeske, and K. Nielsch, "Atomic layer deposition on biological macromolecules: Metal oxide coating of tobacco mosaic virus and ferritin," *Nano Lett.*, vol. 6, no. 6, pp. 1172–1177, 2006.

[106] J. Huang, X. Wang, and Z. L. Wang, "Controlled replication of butterfly wings for achieving tunable photonic properties," *Nano Lett.*, vol. 6, no. 10, pp. 2325–2331, 2006.

[107] M. Knez, K. Nielsch, and L. Niinistö, "Synthesis and surface engineering of complex nanostructures by atomic layer deposition," *Adv. Mater.*, vol. 19, no. 21, pp. 3425–3438, 2007.

[108] H. Kim, H. B. R. Lee, and W. J. Maeng, "Applications of atomic layer deposition to nanofabrication and emerging nanodevices," *Thin Solid Films*, vol. 517, no. 8, pp. 2563–2580, 2009.

[109] M. Ritala, M. Leskelä, E. Nykfinen, P. Soininen, and L. Niinisto, "Growth of titanium dioxide thin films by atomic layer epitaxy," *Thin Solid Films*, vol. 225, pp. 288–295, 1993.

[110] M. Ritala, M. Leskelä, L.-S. Johansson, and L. Niinistö, "Atomic force microscopy study of titanium dioxide thin films grown by atomic layer epitaxy," *Thin Solid Films*, vol. 228, no. 1993, pp. 32–35, 1993.

[111] J. Aarik, A. Aidla, and V. Sammelselg, "Morphology and structure of TiO_2 thin films grown by atomic layer deposition," *J. Cryst. Growth*, vol. 148, pp. 268–275, 1995.

[112] J. Aarik, A. Aidla, V. Sammelselg, and H. Siimon, "Control of thin film structure by reactant pressure in atomic layer deposition of TiO_2 ," *J. Cryst. Growth*, vol. 169, pp. 496-502, 1996.

[113] J. Aarik, A. Aidla, A. Kiisler, and T. Uustare, "Effect of crystal structure on optical properties of TiO_2 films grown by atomic layer deposition," *Thin Solid Films*, vol. 305, pp. 270–273, 1997.

[114] H. Kumagai and M. Matsumotob, "Fabrication of titanium oxide thin films by controlled sequential surface chemical reactions," *Thin Solid Films*, vol. 263, pp. 47–53, 1995.

[115] L. Aarik, T. Arroval, R. Rammula, H. Mändar, V. Sammelselg, and J. Aarik, "Atomic layer deposition of TiO_2 from $TiCl_4$ and O_3," *Thin Solid Films*, vol. 542, pp. 100–107, 2013.

[116] K. Möldre *et al.*, "Atomic layer deposition of rutile and TiO_2 -II from $TiCl_4$ and O_3 on sapphire : Influence of substrate orientation on thin film structure," *J. Cryst. Growth*, vol. 428, pp. 86–92, 2015.

[117] J. Aarik, A. Aidla, T. Uustare, and K. Kukli, "Atomic layer deposition of TiO_2 thin films from TiI_4 and H_2O," *Appl. Surf. Sci.*, vol. 193, pp. 277–286, 2002.

[118] B. K. Kukli *et al.*, "Atomic layer deposition of titanium oxide from TiI_4 and H_2O_2," *Chem. Vap. Deposition*, vol.6, no. 6, pp. 303–310, 2000.

[119] M. Schuisky, J. Aarik, K. Kukli, A. Aidla, and A. Hårsta, "Atomic layer deposition of thin films using O_2 as oxygen source," no. 6, pp. 5508–5512, 2001.

[120] V. Pore *et al.*, "Atomic layer deposition of photocatalytic TiO_2 thin films from TiF_4 and H_2O," *Dalton Trans.*, pp. 6467–6474, 2008.

[121] V. Pore, A. Rahtu, M. Leskelä, M. Ritala, T. Sajavaara, and J. Keinonen, "Atomic layer deposition of photocatalytic TiO_2 thin films from titanium tetramethoxide and water," *Chem. Vap. Deposition*, no. 3, pp. 143–148, 2004.

[122] M. Ritala, M. Leskelä, and E. Rauhala, "Atomic layer epitaxy growth of titanium dioxide thin films from titanium ethoxide," *Chem. Mater.*, no. 7, pp. 556–561, 1994.

[123] J. Aarik, J. Karlis, T. Uustare, and V. Sammelselg, "Influence of structure development on atomic layer deposition of TiO_2 thin films," *Appl. Surf. Sci.*, vol. 181, pp. 339–348, 2001.

[124] A. Rahtu, *Atomic Layer Deposition of High Permittivity Oxides : Film Growth and In Situ Studies*, Ph.D. Dissertation, 2002.

[125] S. K. Kim, W.-D. Kim, K.-M. Kim, C. S. Hwang, and J. Jeong, "High dielectric constant TiO_2 thin films on a Ru electrode grown at 250 °C by atomic-layer deposition," *Appl. Phys. Lett.*, vol. 85, no. 18, p. 4112, 2004.

[126] M. Ritala, M. Leskelä, L. Niinistö, and P. Haussalo, "Titanium isopropoxide as a precursor in atomic layer epitaxy of titanium dioxide thin films," *Chem. Mater.*, vol. 5, no. 8, pp. 1174–1181, 1993.

[127] J. Aarik, A. Aidla, T. Uustare, M. Ritala, and M. Leskela, "Titanium isopropoxide as a precursor for atomic layer deposition: characterization of titanium dioxide growth process," *Appl. Surf. Sci.*, vol. 161, pp. 385–395, 2000.

[128] A. Niskanen, *Radical enhanced atomic layer deposition of metals and oxides*, Ph.D. Dissertation, 2006.

[129] Q. Xie *et al.*, "Atomic layer deposition of TiO_2 from tetrakis-dimethyl-amido titanium or Ti isopropoxide precursors and H_2O," *J. Appl. Phys.*, vol. 102, no. 8, p. 83521, 2007.

[130] G. T. Lim and D. H. Kim, "Characteristics of TiO_x films prepared by chemical vapor deposition using tetrakis-dimethyl-amido-titanium and water," *Thin Solid Films*, vol. 498, no. 1–2, pp. 254–258, 2006.

[131] D. Deduytsche *et al.*, "Growth kinetics and crystallization behavior of TiO [sub 2] films prepared by plasma enhanced atomic layer deposition," *J. Electrochem. Soc.*, no. January, pp. 1–6, 2008.

[132] H. Kang, C. Lee, D. Kim, J. Kim, W. Choi, and H. Kim, "Environmental photocatalytic effect of thermal atomic layer deposition of TiO_2 on stainless steel," *"Applied Catal. B, Environ.*, vol. 104, no. 1–2, pp. 6–11, 2011.

[133] C. Jin *et al.*, "Structure and photoluminescence of the TiO_2 films grown by atomic layer deposition using tetrakis-dimethylamino titanium and ozone," *Nanoscale Res. Lett.*, vol. 10, no. 1, p. 95, 2015.

[134] R. Katamreddy, V. Omarjee, B. Feist, and C. Dussarrat, "Ti source precursors for atomic layer deposition of TiO_2, STO and BST," in *ECS Trans.*, vol. 16, no. 4, pp. 113–122, 2008.

[135] W. J. Maeng and H. Kim, "Thermal and plasma-enhanced ALD of Ta and Ti oxide thin films from alkylamide precursors," *Electrochem. Solid-State Lett.*, vol. 9, no. 6, pp. 191–194, 2006.

[136] Y. Kim and D. Kim, "Atomic layer deposition of TiO_2 from tetrakis-dimethylamido-titanium and ozone," *Korean J. Chem. Eng.*, vol. 29, no. 7, pp. 969–973, 2012.

[137] R. Pheamhom, C. Sunwoo, and D.-H. Kim, "Characteristics of atomic layer deposited TiO_2 films and their photocatalytic activity," *J. Vac. Sci. Technol. A*, vol. 24, no. 4, pp. 1535–1539, 2006.

[138] B. Abendroth *et al.*, "Atomic layer deposition of TiO_2 from tetrakis(dimethylamino) titanium and H_2O," *Thin Solid Films*, vol. 545, pp. 176–182, 2013.

[139] Q. Xie *et al.*, "Atomic layer deposition of TiO_2 from tetrakis-dimethyl-amido titanium or Ti isopropoxide precursors and H_2O," *J. Appl. Phys.*, vol. 102, no. 8, p. 83521, 2007.

[140] J. W. Elam, M. Schuisky, J. D. Ferguson, and S. M. George, "Surface chemistry and film growth during TiN atomic layer deposition using TDMAT and NH_3," *Thin Solid Films*, vol. 436, no. 2, pp. 145–156, 2003.

[141] D. Xie *et al.*, "Atomic layer deposition HfO_2 film used as buffer layer of the $Pt/(Bi_{0.95}Nd_{0.05})(Fe_{0.95}Mn_{0.05})O_3/HfO_2/Si$ capacitors for FeFET application," *J. Adv. Dielectr.*, vol. 1, no. 3, pp. 369–377, 2011.

[142] K. Kukli, J. Aarik, A. Aidla, O. Kohan, T. Uustare, and V. Sammelselg, "Properties of tantalum oxide thin films grown by atomic layer deposition," *Thin Solid Films*, vol. 260, no. 2, pp. 135–142, 1995.

[143] D. H. Kim, W. S. Kim, S. Kim, and S. H. Hong, "Brookite TiO_2 thin film epitaxially grown on (110) YSZ substrate by atomic layer deposition," *ACS Appl. Mater. Interfaces*, vol. 6, no. 15, pp. 11817–11822, 2014.

[144] Y. Yang *et al.*, "The influence of metal interlayers on the structural and optical properties of nano-crystalline TiO_2 films," *Appl. Surf. Sci.*, vol. 258, no. 10, pp. 4532–4537, 2012.

[145] L. Ma, Y. Huang, M. Hou, Z. Xie, and Z. Zhang, "Ag nanorods coated with ultrathin TiO_2 shells as stable and recyclable SERS substrates," *Nat. Publ. Gr.*, pp. 1–8, 2015.

[146] W. Kern and D. A. Puotinen, "Cleaning solutions based on hydrogen peroxide for use in silicon semiconductor technology," *RCA Rev.*, vol. 31, pp. 187–206, 1970.

[147] H. Fujiwara, *Spectroscopic Ellipsometry Principles and Applications*. John Wiley & Sons, 2007.

[148] E. McCafferty and J. P. Wightman, "X-ray photoelectron spectroscopy sputter profile study of the native air-formed oxide film on titanium," *Appl. Surf. Sci.*, vol. 143, no. 1, pp. 92–100, 1999.

[149] A. C. Larson and R. B. Von Dreele, *General Structure Analysis System (GSAS)*, pp. 86–748, 2004.

[150] J. I. Langford and A. J. C. Wilson, "Scherrer after sixty years: A survey and some new results in the determination of crystallite size," *J. Appl. Cryst.*, vol. 11, pp. 102–113, 1978.

[151] C. D. Wagner, "Sensitivity factors for XPS analysis of surface atoms," *J. Electron Spectros. Relat. Phenomena*, vol. 32, pp. 99–102, 1983.

[152] Y. Wang, C. Ma, X. Sun, and H. Li, "Synthesis and characterization of amorphous TiO_2 with wormhole-like framework mesostructure," *J. Non Cryst. Solids*, vol. 319, pp. 109–116, 2003.

[153] V.-S. Dang *et al.*, "Electrical and optical properties of TiO_2 thin films prepared by plasma-enhanced atomic layer deposition," *Phys. Status Solidi A*, vol. 211, no. 2, pp. 416–424, 2014.

[154] ICDD Card No 10706826.

[155] A. Bendavid, P. A. Martin, A. Jamting, and H. Takikawa, "Structural and optical properties of titanium oxide thin films deposited by filtered arc deposition," *Thin Solid Films*, vol. 355–356, pp. 6–11, 1999.

[156] M. T. Aguilar-gama, P. K. Nair, and H. Hu, "Structure and refractive index of thin alumina films grown by atomic layer deposition," *J. Mater. Sci.: Mater. Electron*, vol. 26, pp. 5546-5552, 2014.

CURRICULUM VITAE

PERSONAL INFORMATION

Surname, Name: Aygün, Ezgi
Nationality: Turkish (TC)
Date and Place of Birth: 17th September 1991, Samsun
Marital Status: Married
Phone: +90 312 210 43 03
e-mail: ezgiaygnn@gmail.com

EDUCATION

Degree	Institution	Year of Graduation
MS	METU Micro and Nanotechnology (GPA: 3.79)	2017
BS	Gazi University Chemical Engineering (GPA: 3.23)	2013
High School	Mehmet Emin Resulzade Anadolu High School, Ankara	2009

WORK EXPERIENCE

Year	Place	Enrollment
2015-2017	METU Department of Micro and Nanotechnology	Project Research Assistant
2014-2015	METU Department of Metallurgical and Materials Engineering	Project Research Assistant
July 2013-September 2013	Doğuş Prina Oil Industry and Trade Co.	R&D Engineer
August 2012	ASAŞ Packaging and Printing Industry and Trade Co.	Intern Engineering Student
June 2011	TAI – Turkish Aerospace Industries, Inc.	Intern Engineering Student

PUBLICATIONS

1. **Aygun E.**, Birant G., Polat G., Doganay D., Unalan H. E., and Bek A., "One Dimensional Metal-Dielectric-Metal Nanowires for Plasmonic Applications", to be submitted to Optics Express

2. **Aygun E.**, Nasser H., Ahiboz D., and Bek A. "A Characterization Study on Atomic Layer Deposited TiO_2 Thin Films", to be submitted to Thin Solid Films

3. Ahiboz D., Nasser H., **Aygun E.**, Bek A., Turan R., submitted to IEEE Electron Device Letters

FOREIGN LANGUAGES

- English, TOEFL IBT 104/120
- German, B1 Certificate

HOBBIES

Tennis, Fitness, Books, Movies